

Feature Article: The academic and industrial aspects of the preparation, characterization, mechanical and materials properties, crystallization behavior, melt rheology, and foam processing of pure polylactide (PLA) and PLA/layered silicate nanocomposites are described in this feature article. Recently, these materials have attracted considerable interest in polymer science research. PLA is linear aliphatic thermoplastic polyester and is made from agricultural products. Hectorite and montmorillonite are among the most commonly used smectite-type layered silicates for the preparation of nanocomposites. Smectites are a valuable mineral class for industrial applications because of their high cation exchange capacities, surface area, surface reactivity, adsorptive properties, and, in the case of hectorite, high viscosity, and transparency in solution. In their pristine form, they are hydrophilic in nature, and this property makes them very difficult to disperse into a polymer matrix. The most common way to overcome this difficulty is to replace interlayer cations with quaternized ammonium or phosphonium cations, preferably with long alkyl chains. In general, polymer/layered silicate nanocomposites are of three different types: (1) *intercalated nanocomposites*, in which insertion of polymer chains into the layered silicate structure occurs in a crystallographically regular fashion, regardless of polymer to layered silicate ratio, with a repeat distance of few nanometer; (2) *flocculated nanocomposites*, in which intercalated and stacked silicate layers are sometimes flocculated due to the hydroxylated edge–edge interactions between the silicate layers; (3) *exfoliated nanocomposites*, in which individual silicate layers are uniformly distributed in the

polymer matrix by average distances that totally depend on the layered silicate loading. This new family of composite materials frequently exhibits remarkable improvements in its material properties when compared with those of virgin PLA. Improved properties can include a high storage modulus both in the solid and melt states, increased flexural properties, a decrease in gas permeability, increased heat distortion temperature, an increase in the rate of biodegradability of pure PLA, and so forth.

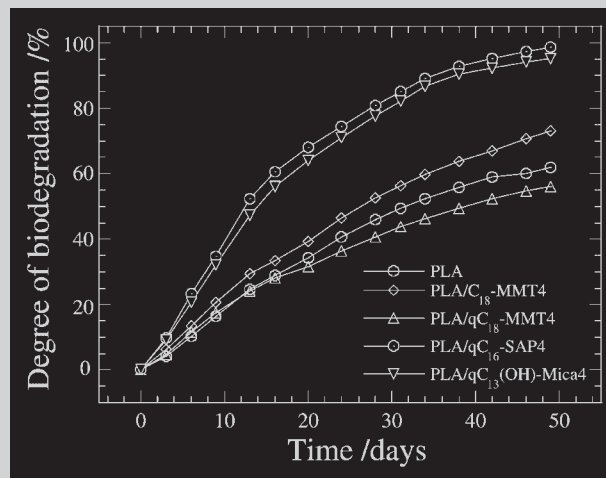


Illustration of the biodegradability of PLA and various nanocomposites.

Biodegradable Polylactide and Its Nanocomposites: Opening a New Dimension for Plastics and Composites

Suprakas Sinha Ray,* Masami Okamoto*

Advanced Polymeric Materials Engineering, Graduate School of Engineering, Toyota Technological Institute, Hisakata 2-12-1, Tempaku, Nagoya 468 8511, Japan

Fax: (+81) 52 809 1864; E-mail: sinharays@toyota-ti.ac.jp; okamoto@toyota-ti.ac.jp

Received: June 20, 2003; Revised: August 19, 2003; Accepted: August 19, 2003; DOI: 10.1002/marc.200300008

Keywords: biodegradable; materials properties; nanocomposites; organically modified layered silicates; polylactide

Introduction

Advanced technology in the field of petrochemical-based polymers has brought many benefits to mankind. However, it is becoming more evident that the ecosystem is considerably disturbed and damaged as a result of the nondegradable plastic materials for disposable items. The environmental impact of persistent plastic wastes is

increasing global concerns, and alternative disposal methods are limited. Incineration of the plastic wastes always produces a large amount of carbon dioxide and creates global warming, and sometimes produces toxic gases, which again contribute to global pollution. On the other hand, satisfactory landfill sites are also limited. Also, the petroleum resources are finite and becoming limited. For this reason, there is an urgent need to develop renewable

source-based environmental benign plastic materials, especially in short-term packaging and disposable applications that would not involve the use of toxic or noxious components in their manufacture and could allow the composting of naturally occurring degradation products. One of the most promising polymers in this direction is PLA because it is made from agricultural products and is readily biodegradable. PLA is not a new polymer; however, recent developments in the manufacturing of the monomer economically from agricultural products have placed this material at the forefront of the emerging biodegradable plastics industries.

PLA is linear aliphatic thermoplastic polyester. High-molecular-weight PLA is generally produced by the ring-opening polymerization of the lactide monomer. Lactide is a cyclic dimer prepared by the controlled depolymerization of lactic acid, which in turn is obtained by the fermentation of corn, sugar cane, sugar beat, and so on.^[1,2] PLA has good mechanical properties, thermal plasticity and biocompatibility, and is readily fabricated, and is thus a promising polymer for various end-use applications.^[3] Even when burned, it produces no nitrogen oxide gases and only one-third of the combustible heat generated by polyolefins, and it does not damage the incinerator and provides significant energy savings.^[4]

So, increasing realization of the various intrinsic properties of PLA, coupled with knowledge of how such properties can be improved to achieve the compatibility with thermoplastics processing, manufacturing, and end-use requirements has fuelled technological and commercial interest in PLA.

Of particular interest is the recently developed nanocomposite technology consisting of a polymer and organically modified layered silicate (OMLS; Figure 1) because they often exhibit remarkably improved mechanical and various other properties as compared with those of virgin polymer.^[5–8] In general, it is believed that these concurrent property improvements in nanocomposites come from interfacial interaction between the polymer matrix and OMLS as opposed to conventional composites.^[9] The layered silicates have layer thickness of the order of 1 nm and a very high aspect ratio (e.g., 10–1 000). A few weight percent of OMLS, which has been properly dispersed throughout the polymer matrix, thus creates much more surface area for polymer/filler interaction than do conventional composites (both micro- and macro-composites).

Ogata et al.^[10] first prepared the blends of PLA and OMLS by a solution casting method but they found only tactoids, which consisted several stacked silicate layers. As a result, the modulus of the blend is slightly higher than that of pure PLA. After that Bandyopadhyay et al.^[11] reported the preparation of intercalated PLA/OMLS nanocomposites with much improved mechanical and thermal properties. Recently, various groups of authors have been interested in the preparation, characterization, and materials properties of PLA/OMLS nanocomposites.^[12]

This paper discusses the nanocomposite technology being used by us to produce various kinds of PLA nanocomposites with much improved mechanical and various other properties. In addition, detail melts rheological characteristics of pure PLA and corresponding nanocomposites, and also behavior towards foam processing will



Dr. Suprakas Sinha Ray studied physical chemistry at the University of Calcutta, India where he received his Master's degree in 1996. In 2000 he completed his Ph.D. thesis at the Department of Chemistry, Presidency College, Calcutta, India under the guidance of Professor Mukul Biswas on the "Preparation and Evaluation of Nanocomposites Based on Some Heterocyclic Polymers". On the basis of his Ph.D. thesis he received a Ph.D. degree in Physical Chemistry (Polymer Science) in early 2001 from the University of Calcutta, India, and then joined Prof. M. Okamoto's polymer physics group at the Toyota Technological Institute, Nagoya, Japan, as a Postdoctoral Fellow. After one year, he received a very prestigious JSPS Postdoctoral Fellowship from the Japanese Government. Presently he is a JSPS Postdoctoral Fellow under the supervision of Prof. Okamoto. He has already published more than 35 papers in highly reputed international journals and about 20 papers in various conference proceedings including two book chapters on various aspects of nanocomposite materials. At present his major research field is the preparation to processing of high performance "green materials".



Dr. Masami Okamoto is an Assistant Professor of the Graduate School of Engineering, Toyota Technological Institute. He received his Ph.D. degree in 1994 from the Tokyo Institute of Technology under the direction of Professor Takashi Inoue on the "Structure Development during Melt Processing and Mechanical Properties in Polymer Blends". He worked at Toyobo Co. where his research program focused on polymer blends and alloys. Following a postdoctoral stay at the National Institute of Advanced Industrial Science & Technology, Kyushu, Japan, he joined the Toyota Technological Institute as a lecturer. Professor Okamoto has established a research program in advanced polymeric nanocomposites and their processing operations. His group's current interests involve the renewable source-based polymeric nanocomposites and the application of these materials to the biodegradable nanocellular polymeric foams by using supercritical carbon dioxide.

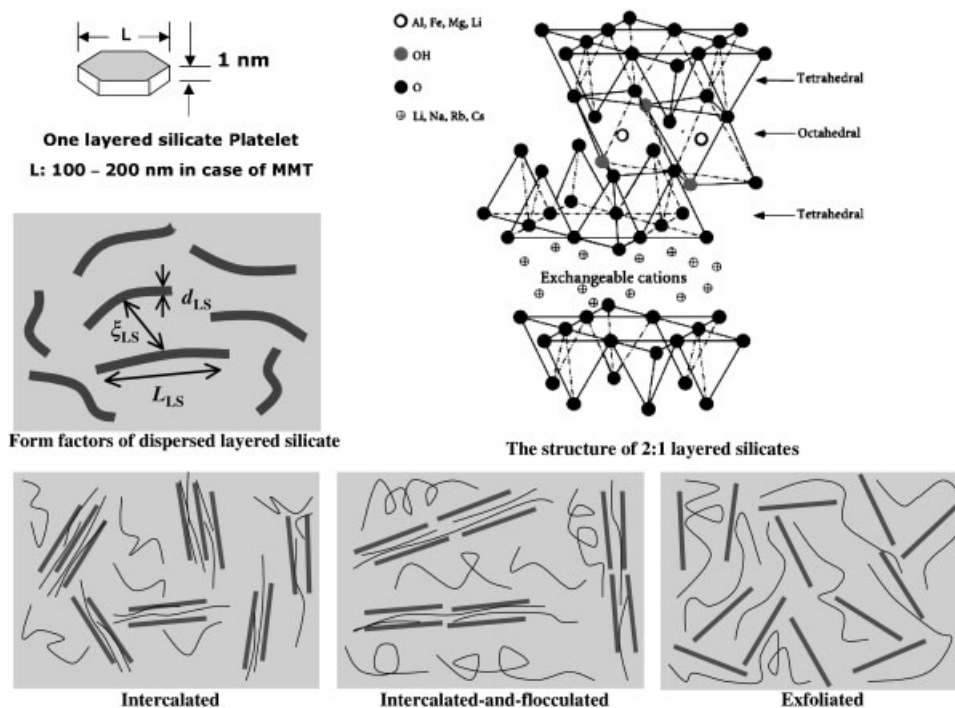


Figure 1. Schematic illustration of three broad classes of thermodynamically achievable polymer/layered silicate nanocomposites.

also be discussed. Finally, attention is drawn to how the biodegradability of pure PLA under compost can be controlled using nanocomposite technology to impart a targeted utility of the final materials.

Experimental Part

Materials

PLA

The conversion of lactide to high-molecular-weight polylactide is achieved by two routes. Recently, Cargill-Dow used a solvent-free process and a novel distillation process to produce a range of polymers.^[13] The essential novelty of the process lies in the ability to go from lactic acid to a low-molecular-weight polylactic acid, followed by controlled depolymerization to produce the cyclic dimer, commonly referred to as lactide. This lactide is maintained in the liquid form and purified by distillation. Catalytic ring-opening polymerization of the lactide intermediate results in the production of PLA with controlled molecular weights. The process is continuous with no necessity to separate the intermediate lactide. A more detailed description of the Cargill-Dow process is illustrated schematically in Figure 2a. In contrast, Mitsui Toatsu (presently Mitsui Chemicals) utilizes a solvent-based process, in which a high-molecular-weight PLA is produced by direct condensation using azeotropic distillation to remove the water of condensation continuously.^[14] Figure 2b illustrates the steps involved in these two processes.

Commercially available PLA grades are copolymers of poly(L-lactide) with *meso*-lactide or D-lactide. The amount of D enantiomers is known to affect the properties of PLA, such as melting temperature, degree of crystallinity and so on. PLA used in this research was supplied by Unitika Ltd. They use the Cargill-Dow method for the production of high-molecular weight PLA. PLA with a D content of 1.1–1.7% was dried under vacuum at 60 °C and kept under dry nitrogen gas for 1 week prior to use.

Organically Modified Layered Silicates

Various kinds of OMLS used in this research were synthesized by replacing Na^+ in different types of layered silicates with alkylammonium or alkylphosphonium cations by ion exchange. In Table 1, we presented detail specifications and designation (as written in the whole text) of five different types of OMLS used in this study.

Nanocomposites Preparation

For nanocomposites preparation, OMLS (powder form) and PLA (pellets form) were first dry-mixed by shaking them in a bag. The mixture was then melt-extruded by using a twin-screw extruder (PCM-30, Ikegai Machinery Co.) operated at 210 °C (screw speed = 100 rpm, feed rate = 120 $\text{gm} \cdot \text{min}^{-1}$) to yield nanocomposite strands. The abbreviation of various nanocomposites (each containing 4 wt.-% of OMLS) is presented in Table 2. The strands were pelletized and dried under vacuum at 60 °C for 48 h to remove water.

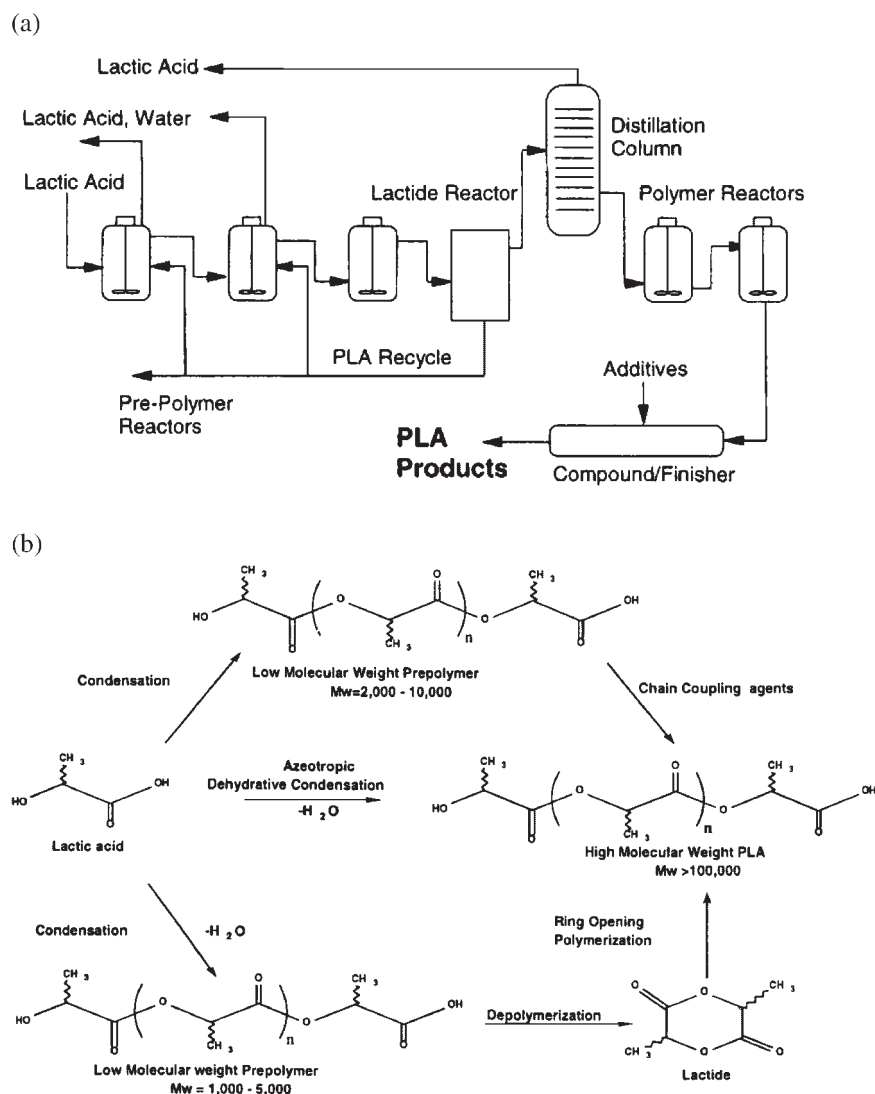


Figure 2. (a) Cargill commercial manufacturing process of PLA (reproduced from reference [2] with permission); (b) Manufacturing routes of polylactic acids (reproduced from reference [2] with permission).

The dried nanocomposite pellets were then converted into sheets with a thickness of 0.7–2 mm by pressing with ~ 1.5 MPa at 190°C for 3 min. The molded sheets were then quickly quenched between glass plates and then annealed

at 110°C for 1.5 h to crystallize isothermally before being subjected to wide-angle X-ray diffraction, transmission electron microscopy, and dynamic mechanical properties measurements.

Table 1. Characteristic parameters and designation of various OMLS.

OMLS code	Pristine layered silicates	Surfactants used for the modification of pristine layered silicates	Particle length	CEC
			nm	meq/100 g ^{a)}
C ₁₈ -MMT	montmorillonite	octadecylammonium cation	~ 150	110
qC ₁₈ -MMT	montmorillonite	dioctadecyldimethylammonium cation	~ 100	90
qC ₁₈ -MMT	montmorillonite	octadecyltrimethylammonium cation	~ 100	90
qC ₁₆ -SAP	saponite	hexadecyltributylphosphonium cation	~ 50	86.6
qC ₁₃ (OH)-mica	synthetic fluorine mica	<i>N</i> -(cocoalkyl)- <i>N,N</i> -[bis(2-hydroxyethyl)]- <i>N</i> -methylammonium cation	200–300	120

^{a)} CEC is the cation exchange capacity and generally expressed as mequiv/100 g.

Table 2. Characteristic parameters of pure PLA and various nanocomposites.

Nanocomposite code ^{a)}	$\bar{M}_w \times 10^{-3}$ g · mol ⁻¹	$\frac{M_w}{M_n}$	T_m °C	T_g °C	T_c °C	χ_c %	$N^{b)} \times 10^5$ μm ⁻¹
PLA	177	1.58	168.2	60.0	127.2	36.0	8
PLA/C ₁₈ -MMT4	161	1.58	169.8	59.2	98.5	49.1	100
PLA/qC ₁₈ -MMT4	163	1.61	170.0	58.6	101.0	47.5	823
PLA/qC ₁₈ -MMT4	163	1.61	169.3	59.7	100.1	65.0	80
PLA/qC ₁₆ -SAP4	149	1.60	168.1	56.0	89.7	39.7	3
PLA/qC ₁₃ (OH)-mica4	150	1.55	168.6	56.0	99.4	40.0	70

^{a)} The number 4 indicates the amount of the corresponding OMLS.

^{b)} N is the primary nucleation density of the spherulites.

Characterization Methods

Wide-Angle X-ray Diffraction (WAXD)

WAXD analyses were performed for the various OMLS powders and corresponding nanocomposite sheets using an MXlabo X-ray diffractometer (MAC Science Co., generator of 3 kW, a graphite monochromator, CuK α radiation (wavelength, $\lambda = 0.154$ nm), operated at 40 kV/20 mA). The samples were scanned in the fixed time (FT) mode with a counting time of 2 s under the diffraction angle 2Θ in the range of 1 to 70°.

Transmission Electron Microscopy (TEM)

To clarify the nanoscale structure of various nanocomposites, conventional TEM (JEM-200CX, JEOL) and high-resolution TEM (H-7100, Hitachi Co.) were also used, and both were operated at an accelerating voltage of 100 kV. The ultra-thin sections either crystallized pellets or sheets (perpendicular to the compression mold) with a thickness of ~ 100 nm were microtomed at -80 °C using a Reichert Ultra cut cryo-ultramicrotome without staining.

Gel Permeation Chromatography (GPC)

The weight-average (\bar{M}_w) and number-average (\bar{M}_n) molecular weights of PLA (before and after nanocomposites preparation) were determined by means of GPC (LC-VP, Shimadzu Co.), using polystyrene standards for calibration and tetrahydrofuran (THF) as the carrier solvent at 40 °C with a flow rate of 0.5 ml · min⁻¹. For the GPC measurements, first PLA or nanocomposites were dissolved in CHCl₃, and then inorganic layered silicates were removed by filtration using a special type of filter, and finally diluted with THF.

GPC results of PLA in the pure state or in OMLS-filled systems are presented in Table 2. As anticipated, the incorporation of various kinds of OMLS resulted in a reduction in the molecular weight of the PLA matrix. Decreased molecular weights of nanocomposites may be explained by either the shear mixing of PLA and OMLS or the presence of hydroxy groups in some modified salt, both resulting in a certain degree of hydrolysis or transesterification reactions of PLA matrix at high temperature.

Differential Scanning Calorimetry (DSC)

The glass transition (T_g), melting (T_m), and crystallization (T_c) temperatures and degree of crystallinity (χ_c) of pure PLA and

various nanocomposites were determined by temperature-modulated DSC (TMDSC) (MDSCTM, TA2920, TA instruments), operated at a heating rate of 5 °C · min⁻¹ with a heating/cooling cycle of the modulation period of 60 s and an amplitude of ± 0.769 °C. For the measurement of χ_c prior to DSC analysis, the extra heat absorbed by the crystallites formed during heating had to be subtracted from the total endothermic heat flow due to the melting of the whole crystallites. This can be done according to the principles and procedures described in our previous paper.^[15] By considering the melting enthalpy of 100% crystalline poly (L-lactide) as 93 J · g⁻¹,^[16] we estimated the value of χ_c of pure PLA and various nanocomposites, and these are presented in Table 2.

Light Scattering (LS) and Polar Optical Micrographic (POM) Observations

To investigate the crystallite texture, the pure PLA and nanocomposite samples were subjected to LS experiments under Hv scattering mode with the radiation of a polarized He-Ne laser of 632.8 nm wavelengths. The details of the LS measurement were described in our previous paper.^[17]

We also observed crystallite growth behavior of pure PLA and various nanocomposites by means of POM. Dried pellets were sandwiched between two glass slides, placed on a laboratory hot plate at 190 °C for 60s to obtain a thin film of ~ 30 μm in thickness. The molten film was then quickly quenched to the desired temperature (110 °C) by putting it on a thermostated hot-stage (Linkam RTVMS, Linkam Scientific Instruments, Ltd.) mounted on a POM (Nikon OPTIPHOTO2-POL). After complete crystallization, the nature of crystallite growth was observed using POM.

Dynamic Mechanical Analysis (DMA)

Dynamic mechanical properties of the pure PLA and various nanocomposites were measured with a Reometrics Dynamic Analyzer (RDAII) in the tension-torsion mode. The temperature dependence of dynamic storage modulus (G'), loss modulus (G''), and $\tan \delta$ of pure PLA and various nanocomposites were conducted at a constant frequency (ω) of 6.28 rad · s⁻¹ with the strain amplitude of 0.05% and in the temperature range of -20 to 160 °C with a heating rate of 2 °C · min⁻¹.

Flexural Properties and Heat Distortion Test

The dried pure PLA and nanocomposite pellets were injection-molded using an injection machine (IS-80G, Toshiba

Machinery Co.) operated at 190 °C with a mold temperature of 30 °C. Flexural modulus and strength of the injection-molded specimens (thickness ~3.2 mm, annealed at 120 °C for 30 min) were measured according to the ASTM D-790 method (Model 2020, Intesco Co.) with a strain rate of 2 mm · min⁻¹ at room temperature (~25 °C). The heat distortion tests of pure PLA and various nanocomposites were conducted using crystallized injection molded samples (Heat Distortion Tester, Toyoseiki Co.) according to the ASTM D-648 method with a heating rate of 2 °C · min⁻¹. We also conducted measurements relating to the load dependence of heat distortion of pure PLA and nanocomposites using the same procedure.

Measurement of Oxygen (O₂) Gas Transmission Rates

O₂ gas transmission rates of pure PLA and various nanocomposites were measured at 20 °C and 90% relative humidity by the ASTM D-1434 differential pressure method (GTR-30XAU, Yanaco Co.). Test samples were prepared by compression molding (thickness ~300 μm) and melt quenched amorphous samples were used for this measurement.

Biodegradability

The biodegradability of neat PLA and various nanocomposites under compost was conducted in two different ways: (a) fragmentation tests; (b) ultimate biodegradability, that is, carbon dioxide (CO₂) evolution.

(a) The fragmentation test of pure PLA and various nanocomposites was studied on a homemade compost instrument at (58 ± 2) °C. The compost used was food waste compost, and was supplied by Japan Steel Works, Ltd. Test specimens were prepared by compression molding with a thickness of 1 mm. The shape of the original test samples (crystallized at 110 °C for 1.5 h) was 3 × 10 × 0.1 cm³.

(b) The degree of biodegradability, that is, CO₂ evolution, was measured directly by means of an attached FT-IR spectrometer (Horiba FT-730). The test specimens were well-crystallized sample pellets, and the compost used was prepared from the mixture of bean-curd refuse, food waste, and cattle feces. This experiment was also conducted at (58 ± 2) °C. We intentionally chose this temperature for both types of biodegradability tests, as the rate of degradation of pure PLA is very slow at ambient temperature.^[1,2]

Melt Rheology

Dynamic shear measurements

Melt rheological measurements were also conducted on RDAII instrument with a torque transducer capable of measurements over the range of 0.2–200 g · cm⁻¹. Dynamic oscillatory shear measurements were performed by applying a time dependent strain of $\gamma(t) = \gamma_0 \sin(\omega t)$ and the resultant shear stress is $\sigma(t) = \gamma_0 [G'(\omega) \sin(\omega t) + G''(\omega) \cos(\omega t)]$, with $G'(\omega)$ and $G''(\omega)$ being the storage and loss modulus, respectively. Measurements were conducted by using a set of 25 mm diameter parallel plates with a sample thickness of ~1.5 mm and in the temperature range of 175–205 °C. The strain amplitude was fixed to 5% to obtain reasonable signal intensities

even at elevated temperature or low ω to avoid the nonlinear response. For each nanocomposite investigated, the limits of linear viscoelasticity were determined by performing strain sweeps at a series of fixed ω s. The master curves were generated using the principle of time-temperature superposition and shifted to a common reference temperature (T_{ref}) of 175 °C, which was chosen as the most representative of a typical processing temperature of pure PLA.

Steady shear measurements

Steady-shear viscosity measurements were conducted at 175 °C using 25 mm diameter cone and plate geometry with a cone angle of 0.1 rad. The steady-shear viscosity data reported in this paper were obtained both as a function of shear rate and time under different shear rates.

Elongation flow rheology

A uniaxial elongational test at constant Hencky strain rate ($\dot{\epsilon}_0$) in the melt state was conducted on a recently developed elongational flow optorheometer,^[18] such as Meissner's new elongational rheometer (commercialized as RME from Rheometric Scientific).^[19] The details of the instrumentation are described elsewhere.^[18]

On each run of the elongation test, samples of 60 × 7 × 1 mm³ sizes were annealed at a predetermined temperature (just above the T_m) for 3 min before starting the run in the rheometer, and uniaxial elongation experiments were conducted at various $\dot{\epsilon}_0$ ranging from 0.01 to 1 s⁻¹.

Foam Processing (Pressure Cell Technique)

Crystallized pure PLA and nanocomposite sheets were first cut into 2 cm × 2 cm pieces and placed in an autoclave connected to a CO₂ cylinder. The samples were then saturated with CO₂ at elevated temperature (140 °C, below the melting point of PLA) and pressure (~10 MPa). Samples were then kept under these conditions for 2 h. Subsequently, the CO₂ was quickly released from the autoclave (within 1 s). After removing the CO₂-saturated pure PLA and nanocomposite sheets from the autoclave, the samples were immersed in a silicon oil bath maintained at the desired temperature (165 °C) for a fixed time (30 s, known as foaming time). The foamed samples were next quenched in an ethanol/water (1:1) mixture, washed in ethanol for at least 30 min., and dried under vacuum at 30 °C for 48 h to remove traces of ethanol and water.

The cellular morphologies of the foamed samples were investigated using a JEOL JSM-5310LV scanning electron microscope (SEM). The samples were freeze-fractured in liquid nitrogen and sputter coated with gold at an argon pressure of 0.1 Torr for 15 min at a current of 15 mA.

The mass density of both prefoamed (ρ_p) and postfoamed (ρ_f) samples in g · cm⁻³ was estimated by using the method of buoyancy. The cell size (d) was obtained by measuring the maximum diameter of each cell perpendicular to the skin. To determine the cell size distribution, the size of at least 75 cells in the core part of the cross section of the fractured-foam sample was measured. The cell densities (N_c) and mean cell-wall thickness (δ) were determined by using Equation (1)

and (2).^[20]

$$N_c \cong \frac{1 - \rho_t/\rho_p}{10^{-4}d^3} \quad (1)$$

$$\delta = d \left(\frac{1}{\sqrt{1 - \rho_t/\rho_p}} - 1 \right) \quad (2)$$

Results and Discussion

Nanocomposite Structure

Generally, the structure of nanocomposites has typically been established using WAXD analysis and TEM observation. Due to the fact that the technique is simple and the apparatus widely available, WAXD is the most frequently used to probe the nanocomposite structure^[5–8] and occasionally to study the kinetics of the polymer melt intercalation.^[21] By monitoring the position, shape, and intensity of the basal reflections from the dispersed silicate layers, the nanocomposite structure (*intercalated* or *exfoliated*) may be identified. For example, in *exfoliated* nanocomposites, the extensive layer separation associated with the delamination of the original silicate layers in the polymer matrix results in the eventual disappearance of any coherent X-ray diffraction from the distributed silicate layers. On the other hand, for *intercalated* nanocomposites, the finite layer expansion associated with the polymer intercalation results in the appearance of a new basal reflection corresponding to the larger gallery height.

Although, WAXD offers a convenient method to determine the interlayer spacing of the silicate layers in the original layered silicates and in the intercalated nanocomposites (within 1–4 nm), little can be said about the spatial distribution of the silicate layers or any structural non-homogeneities in the nanocomposites.^[21] Additionally, some layered silicates initially do not exhibit well-defined basal reflection. Thus, peak broadening and intensity decreases are very difficult to study systematically. Therefore, conclusions concerning the mechanism of nanocomposites formation and their structure based solely on WAXD patterns are only tentative. On the other hand, TEM allows a qualitative understanding of the internal structure, spatial distribution of the various phases, and a view of the defect structure through direct visualization. However, special care must be exercised to guarantee a representative cross section of the sample. Here we combine both WAXD and TEM to determine the final structure of various PLA/OMLS nanocomposites prepared using a simple melt extrusion technique. The intercalation of polymer chains into the silicate galleries usually increases the interlayer spacing of the OMLS, in comparison with the interlayer spacing of the pure OMLS, leading to a shift of the WAXD peak towards the lower value of 2θ .

WAXD patterns for the pure C_{18} -MMT powder and corresponding nanocomposite PLA/ C_{18} -MMT4 are presented in Figure 3a. The mean interlayer spacing of the (001) plane ($d_{(001)}$) for the C_{18} -MMT solid obtained by WAXD measurement is 2.31 nm ($2\theta \cong 3.82^\circ$). In case of PLA/ C_{18} -MMT4, a sharp peak is obtained at $2\theta \cong 2.78^\circ$ ($\cong 3.18$ nm), corresponding to the (001) plane of the dispersed silicate layers in the PLA matrix. This observation indicates the formation of intercalated structure which is not well ordered because the width of the basal reflection of C_{18} -MMT powder is decreased sharply after nanocomposite preparation. From the WAXD patterns, the crystallite

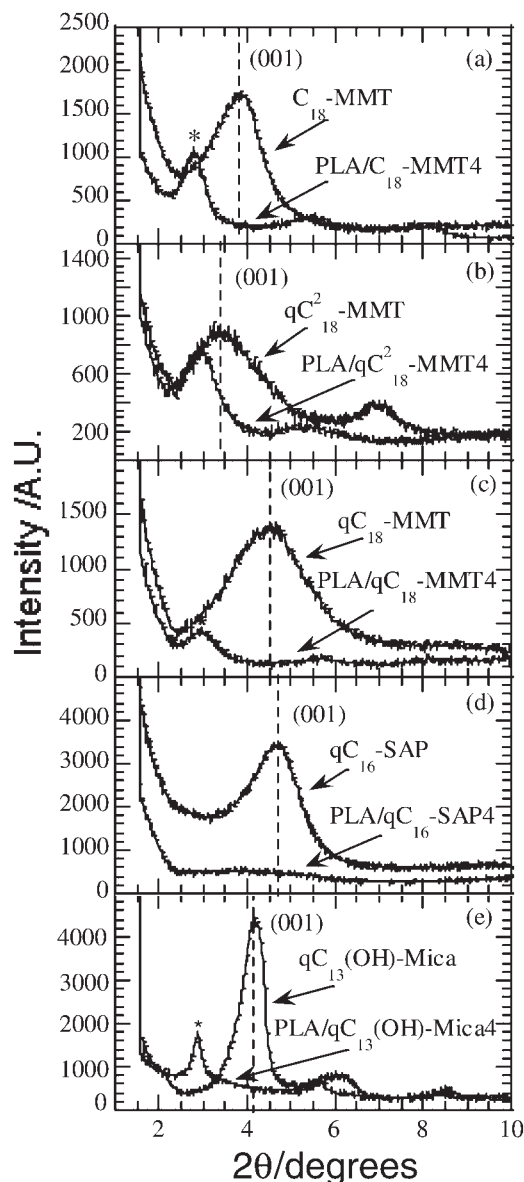


Figure 3. WAXD patterns of pure OMLS powders and corresponding nanocomposite sheets. The dashed line in each panel indicates the location of (001) reflection for OMLS and asterisk indicates the (001) peak of OMLS dispersed in PLA matrix.

size (D) of intercalated and stacked silicate layers of PLA/ C_{18} -MMT4 can roughly be calculated by using Scherrer equation,^[22,23] that is, D is given by Equation (3).

$$D = \frac{k\lambda}{\beta \cos \Theta} \quad (3)$$

k is a constant and generally equal to 0.9, $\lambda = 0.154$ nm, θ is the WAXD peak position, and β is the width of the WAXD peak, and is measured by the full width at half maximum. Since the width of the basal spacing of C_{18} -MMT powder decreased sharply after nanocomposite preparation with PLA, therefore, the coherency of the intercalated silicate layers is much higher than that of the unintercalated. Thus, we can make conclusions on the basis of WAXD analysis that PLA melt intercalation has a strong effect on the layer structure and drastically changes the coherence length of the silicate crystallites.

Figure 4a is a TEM bright field image of PLA/ C_{18} -MMT4, in which the dark entities are the cross section of

stacked intercalated C_{18} -MMT layers and bright areas are the matrix.^[24] From the TEM image, we observed stacked and flocculated silicate layers, which are randomly distributed in the PLA matrix.^[25] Figures 3b and 4b, respectively, represent the WAXD pattern and TEM bright field image of PLA/ qC_{18}^2 -MMT4. The WAXD pattern and TEM observation also represent the stacked and intercalated-and-flocculated structure in the case of PLA/ qC_{18}^2 -MMT4.^[26]

The WAXD patterns of qC_{18} -MMT powder and corresponding nanocomposite PLA/ qC_{18} -MMT4 are shown in Figure 3c. Figure 4c is a bright-field TEM image of an intercalated PLA/ qC_{18} -MMT4. From the WAXD analysis it is confirmed that the extent of intercalation and, at the same time, the disruption of the original silicate crystallite structure occurred to a greater extent in the case of PLA/ qC_{18} -MMT4^[27] than that we observed for PLA/ C_{18} -MMT4^[25] or PLA/ qC_{18}^2 -MMT4.^[26]

Table 3 summarized the form factors (see Figure 1) of various nanocomposites that is, average length (L_{LS}),

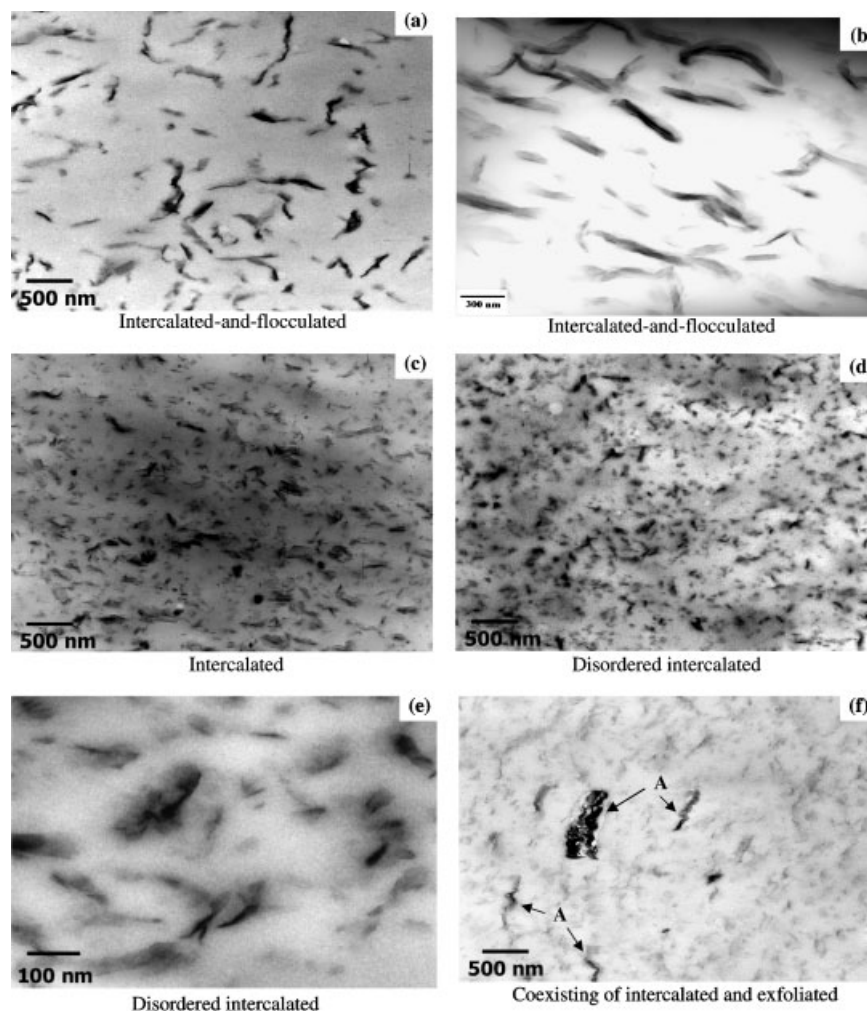


Figure 4. Bright field TEM images of various nanocomposites: (a) PLA/ C_{18} -MMT4; (b) PLA/ qC_{18}^2 -MMT4; (c) PLA/ qC_{18} -MMT4; (d) PLA/ qC_{16} -SAP4; (e) PLA/ qC_{16} -SAP4; (f) PLA/ $qC_{13}(\text{OH})$ -mica4.

Table 3. Form factors of five different nanocomposites obtained from WAXD patterns and TEM observations.

Nanocomposites	PLA/C ₁₈ -MMT4	PLA/qC ₁₈ ² -MMT4	PLA/qC ₁₈ -MMT4	PLA qC ₁₆ -SAP4	PLA/qC ₁₃ (OH)-mica4
WAXD					
d_{001}/nm	3.18	3	3.05	–	3.09 ^{a)}
TEM					
d_{LS}/nm	38 ± 17	60 ± 15	36 ± 19	2–3	1–2
d_{LS}/d_{001}	6.6–17	25–28	9–15	2–3	1–2
L_{LS}/nm	450 ± 200	655 ± 121	200 ± 25	50 ± 5	275 ± 25
ξ_{LS}	260 ± 140	300 ± 52	80 ± 20	70 ± 7	50 ± 5
Structure	intercalated- and-flocculated	intercalated- and-flocculated	intercalated	disorder intercalated	coexisting of intercalated and exfoliated

^{a)} This peak comes from stacked silicate layers present in the nanocomposite structure.

thickness (d_{LS}) of the dispersed stacked intercalated silicate layers and the correlation length (ξ_{LS}) between them. For PLA/C₁₈-MMT4, L_{LS} and d_{LS} are in the range of (450 ± 200) nm and (38 ± 17) nm, respectively. On the other hand, PLA/qC₁₈-MMT4 exhibits almost same level of stacking of the silicate layers ($d_{LS} = (36 \pm 9)$ nm) that we observed in case of PLA/C₁₈-MMT4 with L_{LS} of about (200 ± 25) nm, and is more homogeneously dispersed in the PLA matrix.

Thus, nanocomposite prepared with C₁₈-MMT leads to a much more flocculated structure than that obtained with qC₁₈-MMT. This is due to the hydroxylated edge–edge interaction of the silicate layers.^[25a] Owing to the interaction between the clay particles and PLA matrix, the disk–disk interaction also plays an important role in determining the stability of the clay particles, and hence the enhancement of mechanical properties of such nanocomposites. On the other hand, ξ_{LS} value of PLA/qC₁₈-MMT4 is of the order of (80 ± 20) nm, and is much lower than the value of PLA/C₁₈-MMT4 ((260 ± 140) nm) and PLA/qC₁₈²-MMT4. So, qC₁₈-MMT particles are much more delaminated in the PLA matrix compared with that of C₁₈-MMT or qC₁₈²-MMT particles.

In contrast to PLA/C₁₈-MMT4, PLA/qC₁₈²-MMT4, or PLA/qC₁₈-MMT4, PLA/qC₁₆-SAP4 represents disordered intercalated structure. The WAXD pattern of PLA/qC₁₆-SAP (see Figure 3d) is almost featureless and only exhibits a broad, and extremely weak reflection at approximately $2\theta \cong 3.95^\circ$. In general, many factors other than layer disorder such as intercalate composition, and silicate concentration may contribute to a featureless diffraction.^[21] Thus, on the basis of WAXD patterns it is very difficult to make conclusions about the structure of the nanocomposites exhibiting featureless diffraction patterns. Only the general conclusions about layer order or layer spacing can be inferred. In such cases, TEM is the main tool to determine the exact structure of the nanocomposite.

Figure 4d is a TEM bright-field image of PLA/qC₁₆-SAP4 with comparable magnification to the images of PLA/C₁₈-MMT4 or PLA/qC₁₈-MMT4, respectively. Although, the WAXD pattern is featureless, however, stacking of the

silicate layers is readily observable, and this is more discernible with high magnification TEM photographs (see Figure 4e). We believe this behavior comes from very strong interaction between hexadecyltributylphosphonium salt modified silicate surface and PLA matrix compared with that of alkylammonium salts modified silicate surface and PLA matrix.^[28]

On the other hand, PLA/qC₁₃(OH)-mica4 represents a very sharp WAXD peak (see Figure 3e), indicates the formation of a well-ordered intercalated nanocomposite.^[29,30] Figure 4f show a TEM bright-field image of PLA/qC₁₃(OH)-mica4. From the TEM image it becomes clear that there are some intercalated stacked ('A' in the TEM Figure) and disordered or exfoliated qC₁₃(OH)-mica layers coexisting in the nanocomposite structure. Only the stacked intercalated silicate layers are responsible for very sharp WAXD reflection as observed in Figure 3e, whereas the disordered or exfoliated silicate layers have no periodic stacking and thus remain "silent" in WAXD. This type of mixed intercalated/disordered or exfoliated structure originates from the chemical and size nonhomogeneities of qC₁₃(OH)-mica. Typically the large-in lateral size-qC₁₃(OH)-mica layers create stacked intercalated structure, whereas the smaller layers tend to be disordered or exfoliate.^[29,30]

In order to study polymer/layered silicate nanocomposite structure, WAXD analysis should be always accompanied with TEM investigations, since generally there is coexistence of stacked intercalated, disordered; or exfoliated structures: thus, a sharp WAXD peak not always confirmed a well-intercalated structure (in the case of PLA/qC₁₃(OH)-mica4 system), whereas a featureless WAXD pattern may hide large number of stacked silicate layers (in the case of PLA/qC₁₆-SAP4). In both cases, the materials properties can be dramatically affected by the structures that are not manifested in the WAXD patterns.

Thus, on the basis of WAXD analyses and TEM observations, the authors concluded that four different types of nanocomposites were formed. Ordered intercalated-and-flocculated nanocomposites were obtained when C₁₈-MMT and qC₁₈²-MMT were used as OMLS, intercalated structure

was observed in the case of PLA/qC₁₈-MMT4, PLA/qC₁₆-SAP4 is disordered intercalated, while coexisting stacked intercalated and exfoliated nanocomposite structures were formed in PLA/qC₁₃(OH)-mica4.

Thermal Properties and Crystallite Morphology

Figure 5a shows DSC traces for the melt-quenched samples of pure PLA and various nanocomposites. Samples were prepared using a hot press. These data are obtained from the first run and during the heating process. Samples were first melted at 190 °C, held for three minutes at the same temperature under ~1.5 MPa pressure, and then quickly quenched between the glass plates. From Figure 5a, we can see an endothermic peak for all samples in the temperature range of 55–60 °C. The temperature according to the endothermic peak for each sample is considered to be T_g of PLA. For all samples at T_g there is a steplike change, which is due to the enthalpy relaxation.^[31]

On the other hand, all samples show exothermic peaks and that can be correlated to the crystallization of PLA in every sample; the corresponding temperature is known as

the crystallization temperature, T_c . In the case of nanocomposites this peak is sharper and appeared at lower temperature than that of pure PLA. Therefore, the OMLS hence seems to enhance the crystallization of pure PLA. It should be noted here that T_c does strongly depend upon the nature of OMLS and is much lower in the case of PLA/qC₁₆-SAP4. However, all samples do not show the exothermic peak when annealed at 110 °C for 1.5 h before being subjected to DSC analyses (see Figure 5b). This result indicates PLA matrices were crystallized during heat treatment at 110 °C for 1.5 h.^[32]

POM photographs of pure PLA and five different nanocomposites are presented in Figure 6a. All samples were crystallized at 110 °C beforehand. Pure PLA exhibits a well-defined large crystallite morphology, whereas the sizes of nanocomposites crystallite are significantly smaller. This observation indicates that the surface of dispersed OMLS acts as a nucleating agent for PLA crystallization.

This behavior is more clearly seen in LS patterns (see Figure 6b), in which for nanocomposites, a large smeared four-leaf-clover pattern is observed compared with the crystallized pure PLA, indicating the formation of a large number of poorly organized crystallites. From LS patterns, the number of heterogeneous nuclei N can be estimated from a rough approximation assuming an identical size for all crystallites. The primary nucleation density of the spherulites, that is, N , is given by Equation (4).^[33]

$$N = (3/4\pi)(D_m/2)^{-3} \quad (4)$$

D_m is the maximum diameter of the crystallite, that is, the attainable diameter before impingement. The calculated values of N at 110 °C for pure PLA and various nanocomposites are summarized in Table 2. This phenomenon indicates that the surface of five different types of dispersed OMLS layers act as a nucleating agent for PLA crystallization, which is evident from the increase in the number and density of nuclei causing smaller crystallite formation,^[33] and strongly depends upon the nature of OMLS used for the nanocomposites preparation. In spite of low value of N , PLA/qC₁₆-SAP4 shows acceleration of crystallization at low T_c range (see Figure 5a), which implies that we have to take into account the potentiality of different chain packing with a defect structure. On the other hand, WAXD analysis up to $2\theta = 70^\circ$ indicates a significant peak shift in crystalline chain-chain distance. The larger interchain distance implies the defect-ridden crystallites. Our investigation thus explores the role of OMLS as a nucleating agent for PLA crystallization and we will describe it in a separate section.

Nanocomposites Properties

DMA

DMA measures the response of a given material to an oscillatory deformation (here in tension-torsion mode) as a

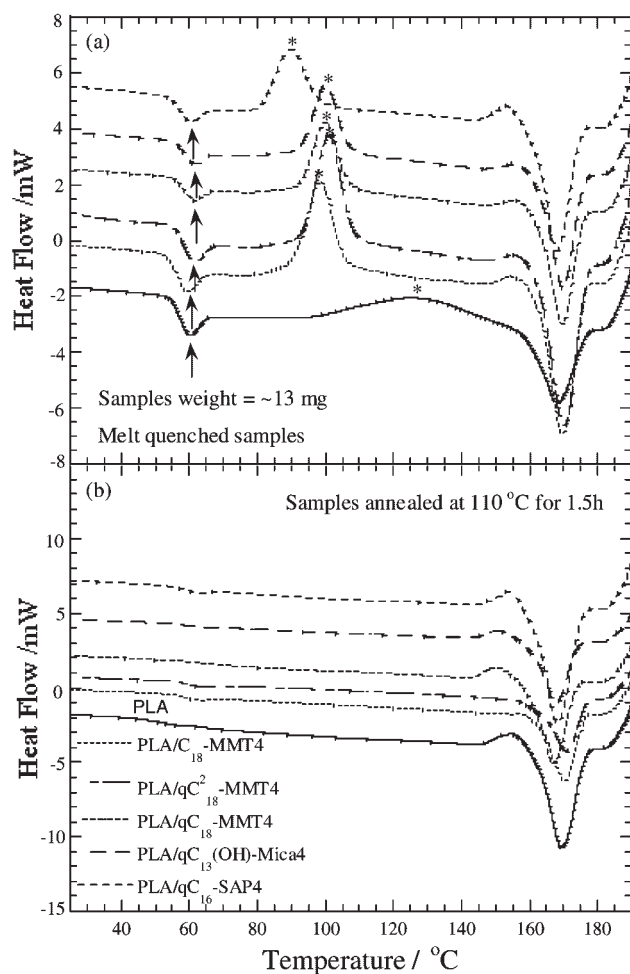


Figure 5. DSC traces of pure PLA and various nanocomposites: (a) melt quenched samples; (b) annealed samples.

function of the temperature. DMA results are expressed in terms of three main parameters: (a) the storage modulus (G'), corresponding to the elastic response to the deformation; (b) loss modulus (G''), corresponding to the plastic response to the deformation; and (c) $\tan \delta$, the G''/G' ratio, useful for determining the occurrence of molecular mobility transitions, such as the glass transition temperature.^[5]

DMA analysis has been used to study the temperature dependence of G' , G'' , and $\tan \delta$ of pure PLA upon nanocomposite formation with five different types of OMLS under different experimental conditions. Figure 7 shows the temperature dependence of G' , G'' and $\tan \delta$ of pure PLA and nanocomposites. For all nanocomposites, the significant enhancement of G' can be seen in the investigated temperature range compared with that of the matrix, indicating all OMLS have a strong influence on the elastic properties of the pure PLA. Below T_g , there is also strong enhancement of G' for all nanocomposites.

In the temperature range of -20 to 0 °C, the increment in G' are 37% for PLA/C₁₈-MMT4, 52% for PLA/qC₁₈-MMT4, 45% for PLA/qC₁₈-MMT4, 31% for PLA/qC₁₆-SAP4, and 23% for PLA/qC₁₃(OH)-mica4 nanocomposites compared with that of pure PLA. Furthermore, in the

temperature range of 80 to 90 °C all nanocomposites exhibit a much higher enhancement of G' (103% for PLA/C₁₈-MMT4, 105% for PLA/qC₁₈-MMT4, 96% for PLA/qC₁₈-MMT4, and 111% for PLA/qC₁₃(OH)-mica4 nanocomposites, as compared with that of pure PLA, with the exception of PLA/qC₁₆-SAP4 with only a 45% increment. This is due to both mechanical reinforcement by silicate particles and extended intercalation. Above T_g , when materials become soft, the reinforcement effect of the silicate particles becomes prominent, due to the restricted movement of the polymer chains, and hence the modulus was greatly enhanced.^[34] The restriction of polymer chains movement by the silicate particles is high in the case of PLA/qC₁₃(OH)-mica4 because of the low value of ξ_{LS} . For this reason, PLA/qC₁₃(OH)-mica4 shows a high increment in G' at high temperature compared with that of other nanocomposites. At room temperature (~ 25 °C), PLA/C₁₈-MMT4, PLA/qC₁₈-MMT4, PLA/qC₁₈-MMT4, and PLA/qC₁₆-SAP4 exhibited higher increments in G' of 38%, 44%, 51%, and 30%, respectively, as compared with that of pure PLA, whereas PLA/qC₁₃(OH)-mica4 shows only a 26% increment.

On the other hand, above T_g the enhancement of G'' is significant in the intercalated nanocomposites compared

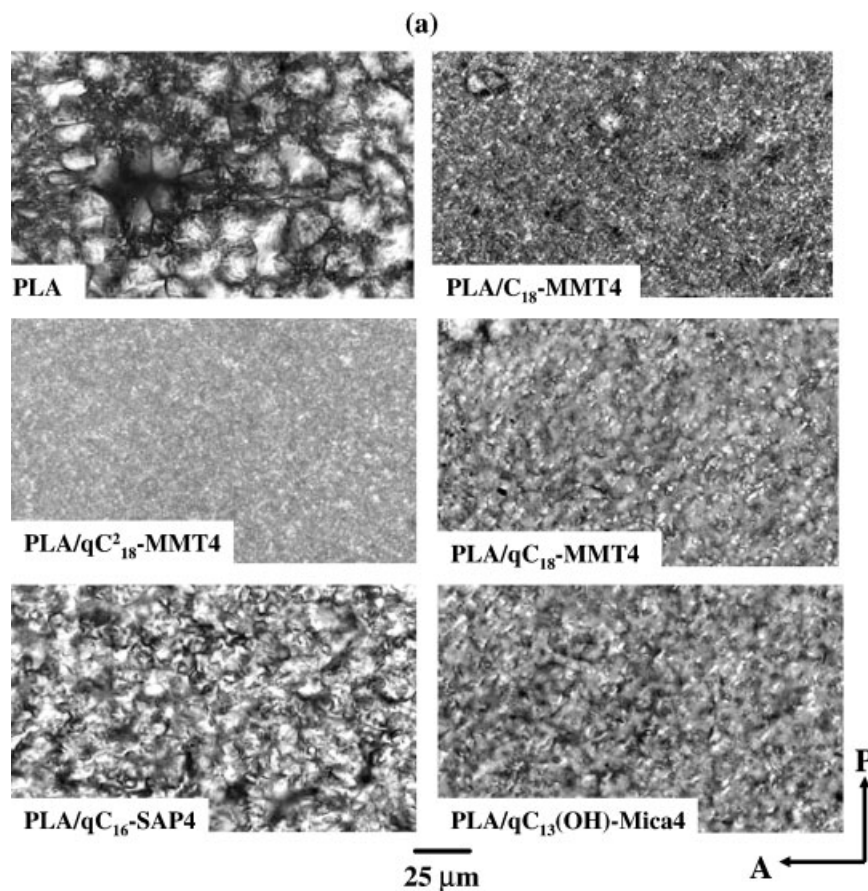


Figure 6. (a) Polarized optical micrographs of crystallized samples of pure PLA and various nanocomposites; (b) corresponding Hv-light scattering patterns.

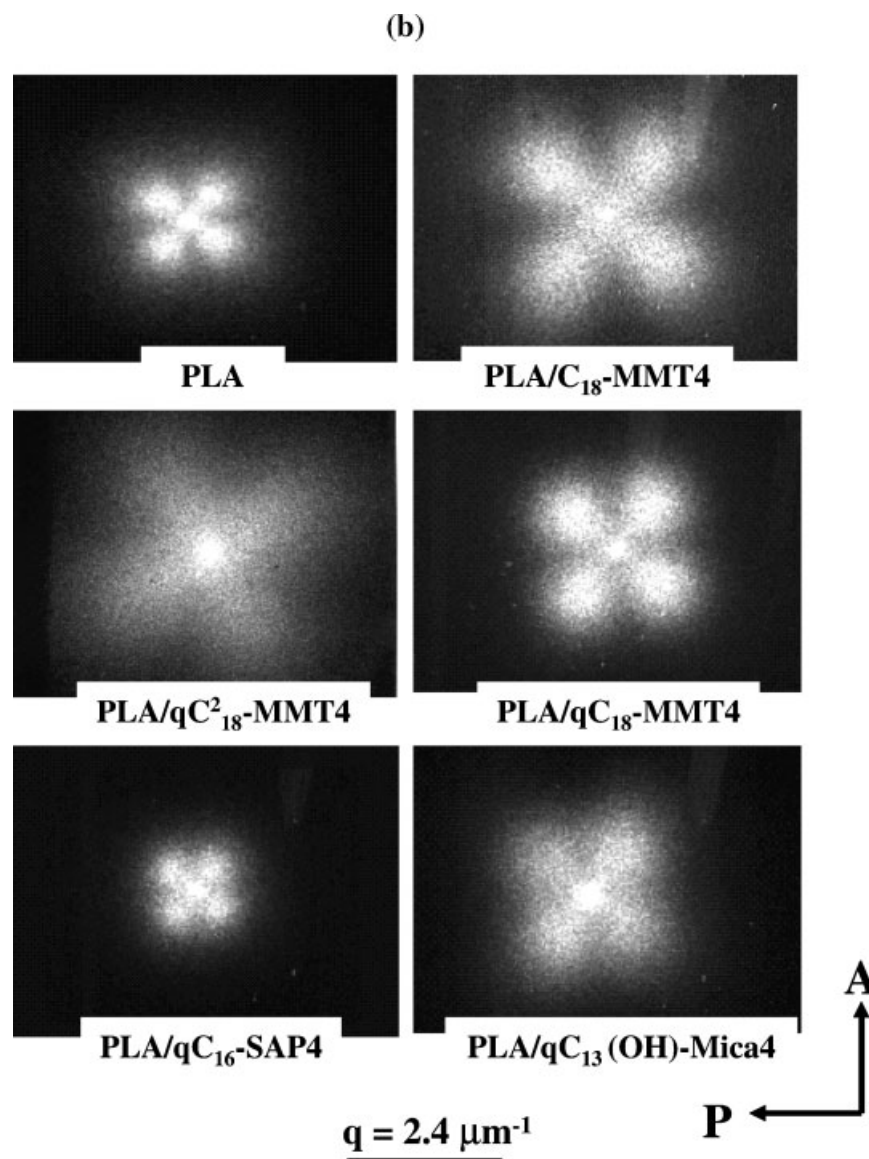


Figure 6. (Continued)

with that of below T_g indicating the plastic response to the deformation of pure PLA is prominent in the presence of OMLS when the materials become soft. However, the presence of OMLS does not lead to a significant shift and broadening of the $\tan \delta$ curves for all nanocomposites compared with that of pure PLA. This behavior has been ascribed to the restricted segmental motions in the organic–inorganic interfaces neighborhood of intercalated nanocomposites.

Flexural Properties

In Table 4, we report the flexural modulus and strength of pure PLA and various nanocomposites measured at 25 °C. There is a significant increase in the flexural modulus for all nanocomposites except PLA/qC₁₆-SAP4 compared with

that of pure PLA. The high value of modulus in the case of PLA/qC₁₃(OH)-mica4 and low value of modulus in the case of PLA/qC₁₆-SAP4 may be due to the different aspect ratio of the dispersed OMLS in the PLA matrix (see Table 3). On the other hand, flexural strength is also remarkably increased in the case of PLA/C₁₈-MMT4, PLA/qC₁₈-MMT4, or PLA/qC₁₈²-MMT4 nanocomposites, but there is not so much of an increase in the case of PLA/qC₁₃(OH)-mica4 or PLA/qC₁₆-SAP4 nanocomposites. This behavior may be due to the presence of qC₁₃(OH)-mica or qC₁₆-SAP, which leads to a brittleness of nanocomposites as revealed by their distortion value (see Table 4).

Heat Distortion Test

The nanodispersion of OMLS in PLA matrix also promotes a higher heat distortion temperature (HDT). We examined

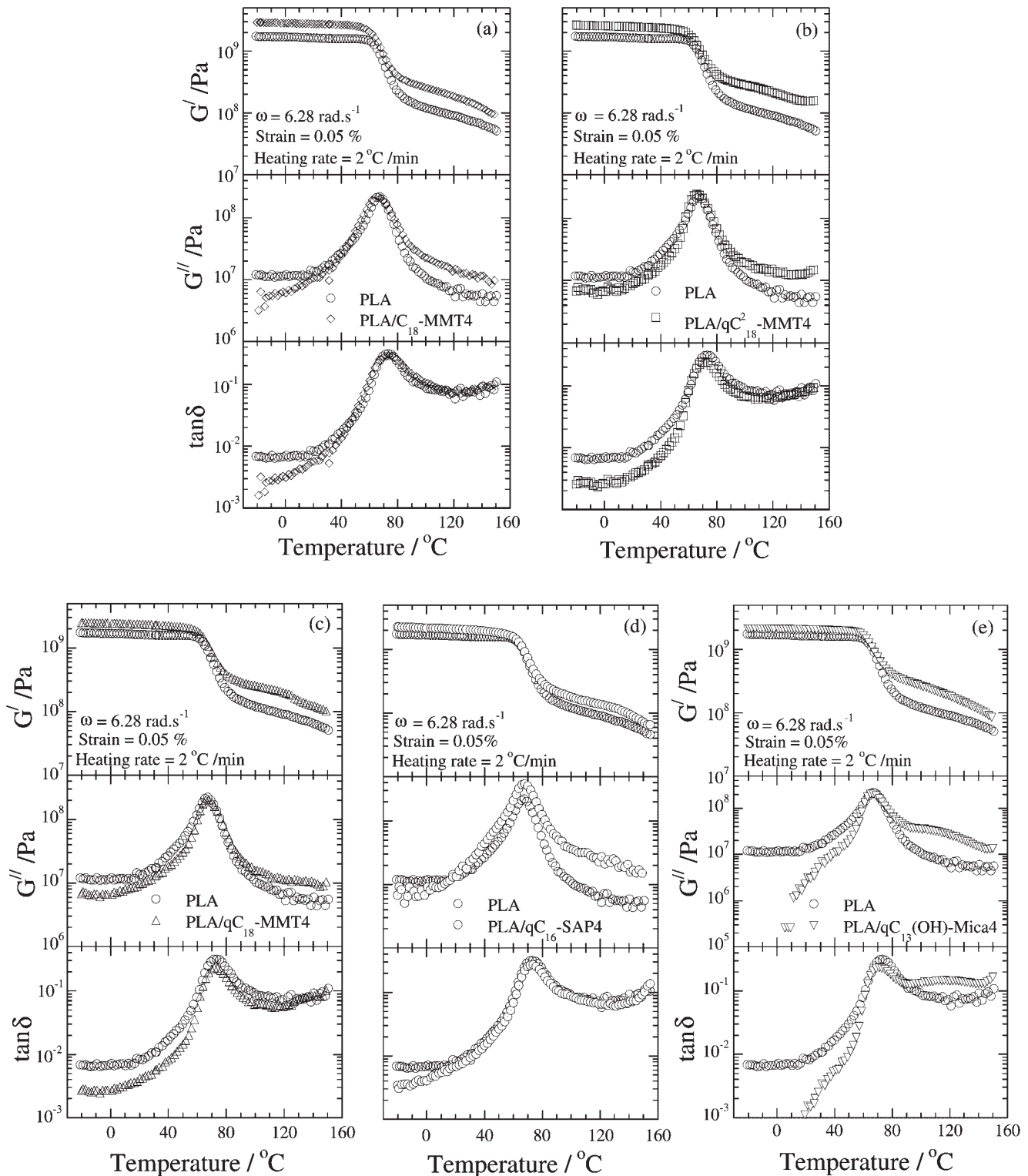


Figure 7. Temperature dependence of storage modulus (G'), loss modulus (G''), and $\tan \delta$ of pure PLA and corresponding nanocomposites: (a) PLA/C₁₈-MMT4; (b) PLA/qC₂-MMT4; (c) PLA/qC₁₈-MMT4; (d) PLA/qC₁₆-SAP4; (e) PLA/qC₁₃(OH)-Mica4.

the HDT of pure PLA and various nanocomposites with different load conditions. As seen in Table 4, in the case of nanocomposites, there is a marked increase in HDT with intermediate load of 0.98 MPa, from 76 °C for the pure PLA

to 98 °C for PLA/qC₁₆-SAP nanocomposite. In the case of PLA/qC₁₆-SAP4, the value of T_m (see Table 2) does not change significantly as compared with that of pure PLA. Furthermore, in WAXD analysis up to $2\theta \cong 70^\circ$, we

Table 4. Comparison of practical materials properties of pure PLA and various nanocomposites.

Practical materials properties	PLA	PLA/ C ₁₈ -MMT4	PLA/ qC ₁₈ ² -MMT4	PLA/ qC ₁₈ -MMT4	PLA/ qC ₁₆ -SAP4	PLA/ qC ₁₃ (OH)-mica4
Flexural modulus/GPa at 25 °C	4.84	5.66	5.43	5.57	4.5	6.11
Flexural strength/MPa at 25 °C	86	132	102	134	93	94
Distortion at break/%	1.9	3.2	3.9	3.1	1.5	1.5
HDT/°C with 0.98 MPa load	76	94	91.3	93	98	93
O ₂ gas permeability (ml · mm/m ² · day · MPa)	200	172	171	177	120	71
O ₂ gas permeability (ml · mm/m ² · day · MPa) ^{a)}	200	180	181	188	169	68

^{a)} Calculated on the basis of Nielsen theoretical equations (Equation (5) and (6) in the text).

observed significant shifting of the peaks in the crystallized PLA/qC₁₆-SAP4 sample. The strong improvement of HDT in the case of PLA/qC₁₆-SAP4 may be originated from the formation of another crystal structure.

On the other hand, imposed load dependence on HDT is clearly observed in the case of nanocomposites. Figure 8 shows the typical load dependence in the case of pure PLA and various nanocomposites each containing 7 wt.-% of corresponding OMLS. From Figure 8, we can see in the very low or high region there is almost no increment in HDT in the case of nanocomposites compared with that of pure PLA. But with intermediate load, all nanocomposites show significant improvement in HDT compared with that of pure PLA. In the case of nanocomposites with high or low load, it is very difficult to achieve high HDT improvement without strong interaction between polymer matrix and OMLS. For all nanocomposites studied here, the values of T_m (see Table 2) do not change significantly as compared with that of pure PLA. Furthermore, in WAXD analyses of crystallized samples up to $2\theta \cong 70^\circ$, we do not observe significant shifting or formation of new peaks in the crystallized nanocomposite samples. Thus, the improvement

of HDT with intermediate load (0.98 MPa) originates from the better mechanical stability of nanocomposites or is due to the mechanical reinforcement by the dispersed silicate particles, higher value of χ_c , and intercalation.^[33] This is qualitatively different from the behavior of nylon-6/OMLS nanocomposites; there is a strong interaction between the layered silicates and the nylon-6 matrix by forming hydrogen bonding.^[35] The increase in HDT of pure PLA due to the nanocomposites preparation is a very important property improvement, not only from the industrial point of view but also from molecular level control on the silicate layers, that is, crystallization through interfacial interaction between PLA molecules and SiO₄ tetrahedral layers.

O₂ Gas Permeability

Layered silicates are believed to increase the gas barrier properties by creating a maze or “*tortuous path*” (see schematic illustration in Figure 9) that retard the progress of gas molecules through the matrix resin.^[5,27,30] The O₂ gas permeability coefficient for the pure PLA and various nanocomposites are presented in Table 4. According to the Nielsen model, for platelets of length ($\cong L_{LS}$) and width ($\cong d_{LS}$) of the layered silicate, which are dispersed parallel in polymer matrix, the tortuosity factor (τ) can be expressed as in Equation (5).^[36]

$$\tau = 1 + (L_{LS}/2d_{LS})\phi_{LS} \quad (5)$$

ϕ_{LS} is the volume fraction of dispersed layered silicate particles (inorganic part). Therefore, the relative permeability coefficient (P_{PLACN}/P_{PLA}) is given by Equation (6).

$$\frac{P_{PLACN}}{P_{PLA}} = \frac{1}{1 + (L_{LS}/2d_{LS})\phi_{LS}} \quad (6)$$

P_{PLACN} and P_{PLA} are the permeability coefficient of nanocomposite and pure PLA, respectively. We consider here the PLA/qC₁₈-MMT4 system in order to prove the validity of the above model in the case of these nanocomposites, with value of $L_{clay} \cong \sim 200$ nm (average value from TEM, Table 3), and the value of $d_{LS} \cong \sim 36$ nm as calculated from TEM photograph. Therefore, the calculated value of

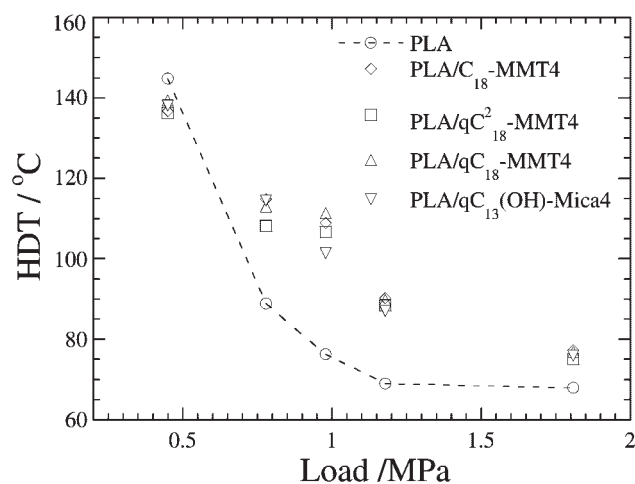


Figure 8. Load dependence of HDT of pure PLA and various nanocomposites (each containing 7 wt.-% of OMLS).

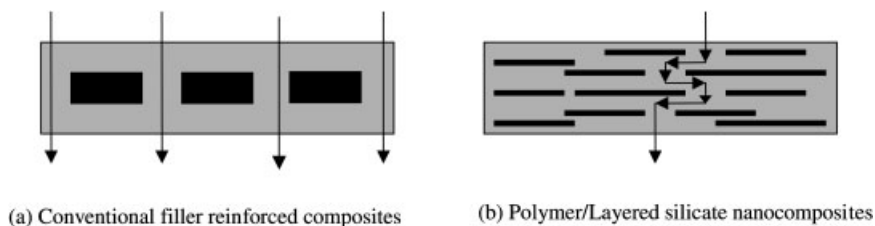


Figure 9. Schematic illustration of formation of "tortuous path" in nanocomposite.

$P_{\text{PLACN}}/P_{\text{PLA}}$ for PLA/qC₁₈-MMT4 is equal to 0.94. The experimental value of 0.88 is almost well matched with the above model but slightly lower than the calculated one. Presumably, the planer orientation of the dispersed silicate particles in the compression-molded sheet is not sufficient.

The gas barrier property of nanocomposites primarily depends on two factors: one is the dispersed layered silicate particles dimension and other is the dispersion of layered silicate in polymer matrix.^[5] When the degree of dispersion of layered silicate in the matrix is the same, the barrier property directly depends upon the dispersed layered silicate particles dimension, that is, the aspect ratio.

According to the above theoretical expression as described in Equation 6, we have estimated the O₂ gas transmission coefficient using the experimentally obtained $L_{\text{LS}}/d_{\text{LS}}$ value as summarized in Table 3. Among the five nanocomposites, the calculated values are almost matched with the experimental values, with the exception of PLA/qC₁₆-SAP4 system (see Table 4), which shows a higher value of the permeability coefficient despite the much lower aspect ratio compared with that of other systems.

Gusev et al.^[37] considered another factor, which is also responsible for the barrier property: changes in the local permeability due to the molecular level of transformation in the polymer matrix in the presence of silicate layers. This factor is directly related to the molecular level interactions of polymer matrix with the silicate layers. The PLA/qC₁₆-SAP4 is a disordered intercalated system, the favorable interactions between PLA and silicate layers are probably due to the formation of phosphonium oxide caused by the reaction between the hydroxy end group of PLA and the alkylphosphonium cation. As a result, the barrier property of PLA/qC₁₆-SAP4 is much higher compared with that of other systems.^[38]

Biodegradability

More exciting aspect of this research is the enhanced biodegradability of pure PLA after nanocomposites preparation. A major problem with the PLA matrix is the slow rate of degradation as compared with the rate of waste accumulation. Despite the considerable number of reports concerning the enzymatic degradation of PLA^[39,40] and various PLA blends,^[41] there is very little known about the compost degradability of PLA,^[1,2] except in recent

publications by the present authors.^[27,29,38,42–44] Figure 10a represents the real picture of recovered samples from compost with time. The decreased \bar{M}_w and residual weight percentage (R_w) of the initial tests samples with time are also reported in Figure 10b and c, respectively. Based on Figure 10, there is no significant discrepancy between PLA/C₁₈-MMT4 and PLA/qC₁₈-MMT4, though only the latter is pointed out as enhancer of the biodegradability. Within one month, both the extent of \bar{M}_w and the extent of weight loss are almost the same for both pure PLA and PLA/qC₁₈-MMT4. However, after one month, a sharp change occurs in the weight loss of PLA/qC₁₈-MMT4, and within two months, it is completely degraded in compost.

We also conducted a respirometric test to study the degradation of the PLA matrix in a compost environment.^[29,30,38] For this test the compost used was prepared from the mixture of bean-curd refuse, food waste, and cattle feces. Unlike weight loss or fragmentation, which reflects the structural changes in the test sample, CO₂ evolution provides an indicator of the ultimate biodegradability, that is, mineralization, of the test samples. In Figure 11a we report the time-dependence biodegradation (i.e. CO₂ evolution) of pure PLA and various nanocomposite samples. These data clearly indicate that the biodegradability of the PLA component in PLA/qC₁₃(OH)-mica4 or PLA/qC₁₆-SAP4 was enhanced significantly. On the other hand, PLA component in PLA/C₁₈-MMT4 shows a slightly higher biodegradation rate, while the rate of degradation of pure PLA and PLA/qC₁₈-MMT4 is almost the same level. The compost degradation of PLA occurs by a two-step process. During the initial phases of degradation, the high-molecular-weight PLA chains hydrolyze to lower molecular weight oligomers. This reaction can be accelerated by acids or bases and is also affected by both temperature and moisture. Fragmentation of the plastic occurs during this step at a point where the \bar{M}_n decreases to less than about 40 000. At about this same \bar{M}_n , microorganisms in the compost environment continue the degradation process by converting these lower molecular weight components to CO₂, water, and humus.^[1,2] Therefore, any factor, which increases the hydrolysis tendency of the PLA matrix ultimately controls the degradation of PLA.

The incorporation of OMLS fillers into the PLA matrix resulted in a small reduction in the molecular weight of the matrix (see Table 2). It is well known that PLA of relatively

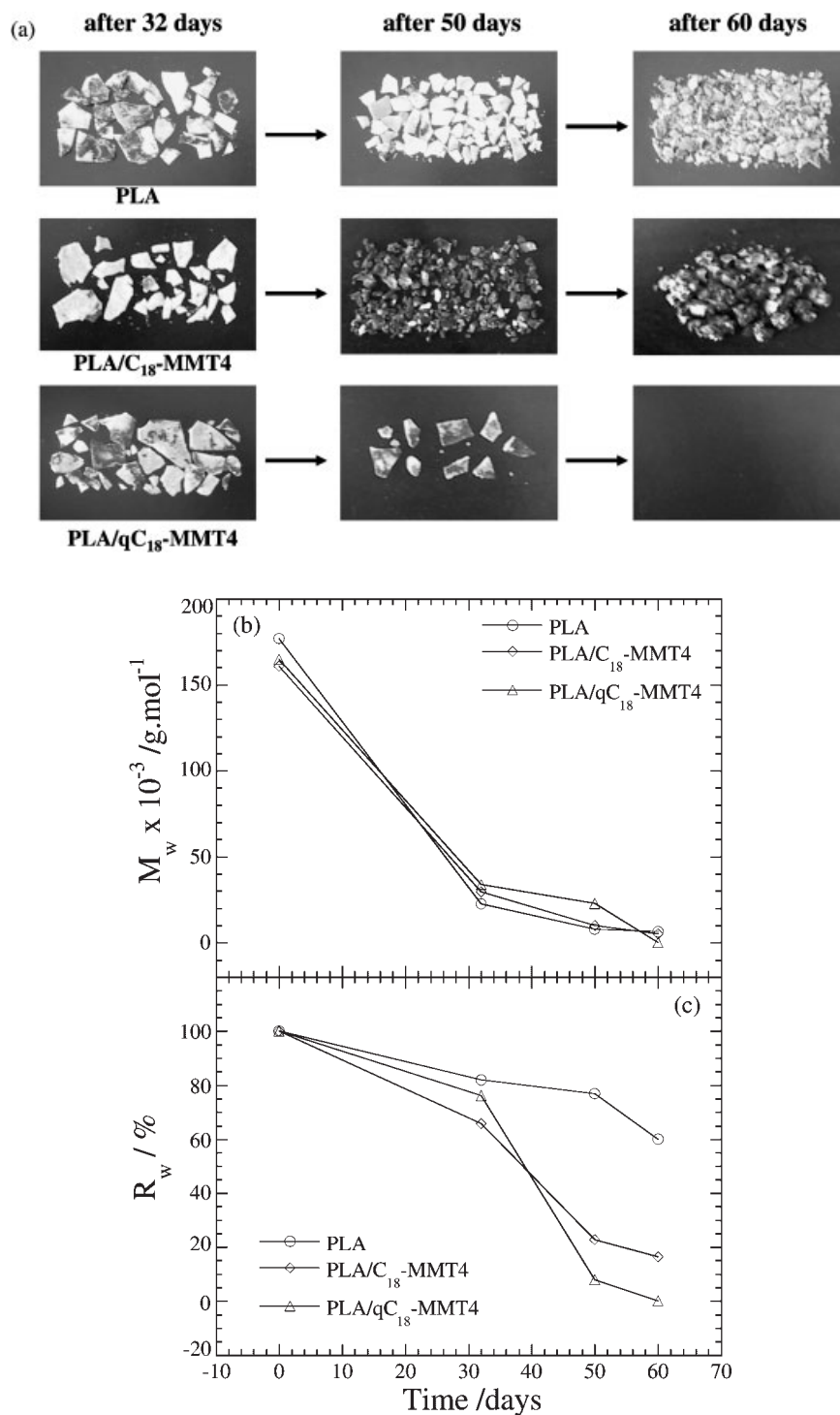


Figure 10. (a) Real picture of biodegradability of pure PLA and two different nanocomposites recovered from compost with time. The initial shape of the crystallized samples was $3 \times 10 \times 0.1 \text{ cm}^3$; (b) Time-dependent change of matrix \bar{M}_w of pure PLA and corresponding nanocomposites under compost; (c) Time-dependent weight percentage (R_w) of pure PLA and two different nanocomposites.

lower molecular weight may show higher rates of enzymatic degradation because of, for example, the high concentration of accessible chain end groups.^[45] However, in these cases the rate of molecular weight change of pure

PLA and PLA in various nanocomposites is almost the same (see Figure 10b and Figure 11b). So the initial molecular weight is not a main factor here for controlling the biodegradability of nanocomposites. Another factor that controls

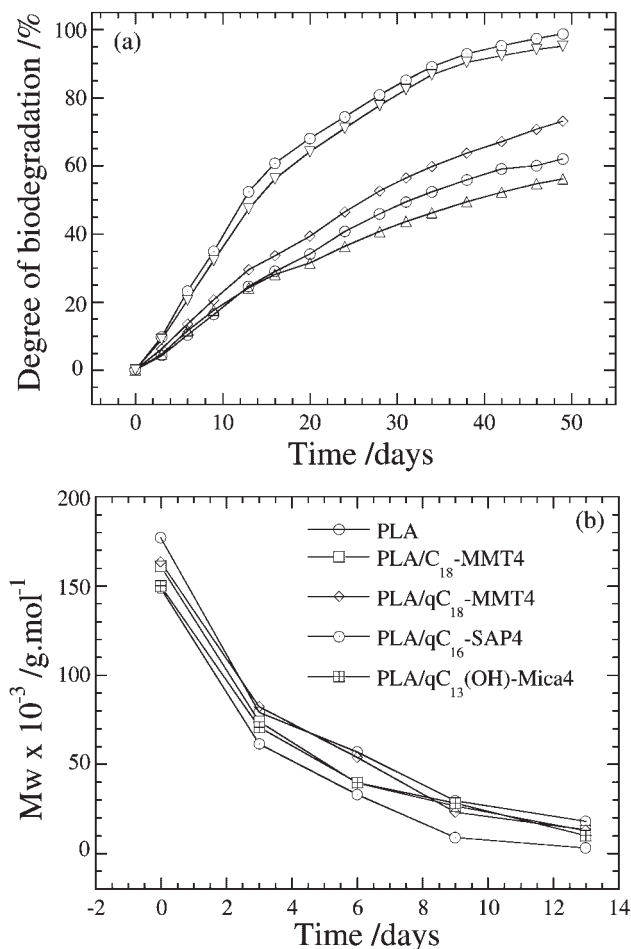


Figure 11. Time dependence of (a) degree of biodegradation (i.e. CO₂ evolution); (b) change of matrix \bar{M}_w of pure PLA and corresponding nanocomposites under compost.

the biodegradability of PLA is the χ_c value because the amorphous phase is easy to degrade compared with that of the crystal phase.^[39,40] In Table 2, we show the χ_c value of the pure PLA sample is lower than that of nanocomposite samples except for PLA/qC₁₆-SAP4 and PLA/qC₁₃(OH)-mica4. These two nanocomposite samples do not enhance the degree of crystallinity.

These data indicate that the incorporation of different types of OMLS in the PLA matrix resulted in a different mode of attack on the PLA component of the test samples that might be due to the presence of different kinds of modified salts and pristine layered silicates. Since PLA is an aliphatic polyester, it is conceivable that incorporation of different types of OMLS resulted in a different mode of disruption of some of the ester linkages due to the presence of different kinds of surfactants and layered silicates. The disruption of ester bonds is more facile in presence of qC₁₃(OH)-mica or qC₁₆-SAP and less facile with qC₁₈-MMT. Therefore, our investigation explores the role of OMLS as nanofiller to enhance the rate of biodegradation of

pure PLA, and we can control the biodegradability of PLA by judicious choice of OMLS.

Crystallization Behavior

In the previous sections we have reported the preparation, characterization, mechanical, and various materials properties, and biodegradability of pure PLA and five different nanocomposites. In all cases, intrinsic properties of pure PLA were concurrently improved after nanocomposites preparation with five different types of OMLS. But if we want to control the mechanical and various other properties of pure PLA before and after nanocomposite preparation, we have to know the crystallization behavior of pure PLA in detail and also how it is affected in the presence of OMLS. The main objective of this section is to understand the effect of OMLS on the crystallization kinetics, and crystallization structure and morphology of pure PLA upon nanocomposite formation with OMLS. In order to understand these we chose PLA/C₁₈-MMT4 as a representative system and describe the crystallization behavior in detail.

To understand the crystallization kinetics of pure PLA before and after nanocomposite preparation at low T_c (≤ 120 °C), we have used time-resolved LS photometry, which is a powerful tool for estimating the overall crystallization rate and its kinetics in super cooled crystalline polymer liquid.^[46] Details regarding LS experiments are described elsewhere.^[47,48] For the kinetics of crystallization, we can employ the integrated scattering intensity, that is, the invariant Q , defined as in Equation (7).

$$Q = \int_0^\infty I(q)q^2 dq \quad (7)$$

q (scattering vector = $(4\pi/\lambda_{LS}) \sin(\theta_{LS}/2)$) and $I(q)$ is the intensity of the scattered light at q .^[49]

In the Hv mode, the invariant Q_δ can be described by the mean-square optical anisotropy $\langle \delta^2 \rangle$ [Equation (8)].

$$Q_\delta \propto \langle \delta^2 \rangle \propto \phi_s (\alpha_r - \alpha_t)^2 \quad (8)$$

ϕ_s is the volume fraction of spherulites, and α_r and α_t are the radial and tangential polarizabilities of spherulites, respectively. We constructed a plot of reduced invariant Q_δ/Q_δ^∞ versus time t with Q_δ^∞ being Q_δ at an infinitely long time of crystallization (up to full solidification of the melt).

Figure 12 shows the time variation of the invariant Q_δ/Q_δ^∞ taken for pure PLA and PLA/C₁₈-MMT4 at 110 °C. The overall crystallization rate was determined from the slope of Q_δ/Q_δ^∞ ($d(Q_\delta/Q_\delta^\infty)/dt$) in the crystallization region as indicated by the solid line in Figure 12, and is plotted in Figure 13. It is clear that the overall crystallization rate increases in PLA/C₁₈-MMT4, in comparison to the pure PLA, as well as the rate increases in the case of PLA/C₁₈-MMT4 for a particular T_c . The same trend is also observed over the wide range of T_c studied here. Here it should be mentioned that the equilibrium melting temperatures (T_m^0)

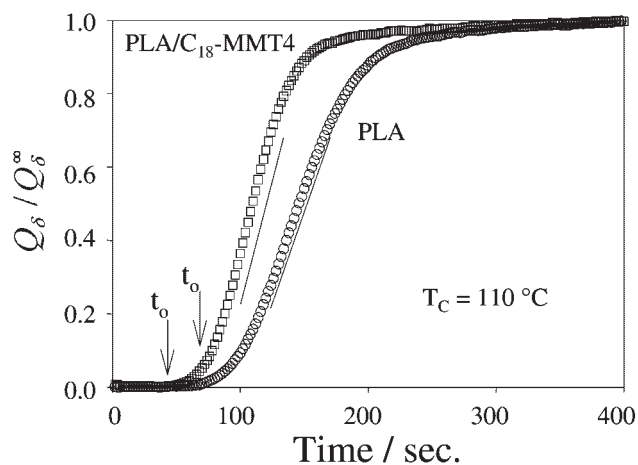


Figure 12. Time variation of reduced invariant Q_δ/Q_δ^∞ during isothermal crystallization at quiescent state at $T_c = 110^\circ\text{C}$. The solid line represents the slope (overall crystallization rate).

of the PLA/C₁₈-MMT4 and pure PLA are the same. The T_m^0 s were measured by isothermal crystallization at various temperatures by carrying out a Hoffman–Weeks^[50] plot as shown in Figure 14. Both PLA/C₁₈-MMT4 and pure PLA show the same value of T_m^0 of 179.54°C and that would nullify the effect of super cooling $\Delta T (\equiv T_m^0 - T_c)$ on the overall crystallization rate, linear growth rate, G , and so on. The overall crystallization rate with T_c is typical rate curve as usual for semicrystalline polymers.^[51] However, the rate of PLA/C₁₈-MMT4 is enhanced for every temperature of measurement, especially at higher T_c s. From the onset time t_0 we can estimate the induction time of the crystallization until the start of crystallization. The observed value of t_0 at 110°C was 74 s for pure PLA and 56 s for PLA/C₁₈-MMT4. At all T_c measured here, the t_0 value for PLA/C₁₈-MMT4 is always lower than that of pure PLA. This reduction of t_0 in the case of the nanocomposite is attributed to the presence of C₁₈-MMT particles as a nucleating agent.

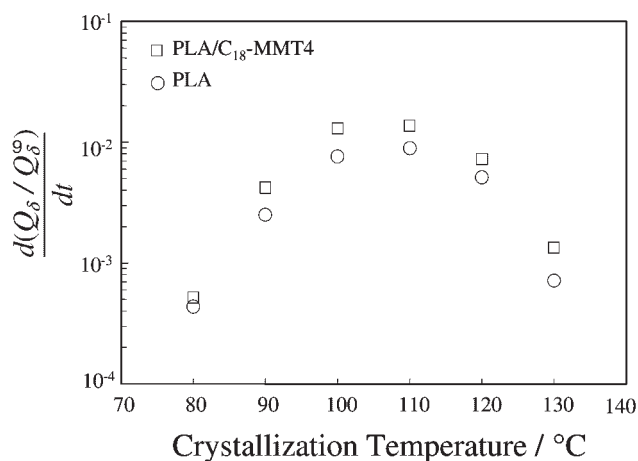


Figure 13. T_c dependence of the overall crystallization rate of pure PLA and PLA/C₁₈-MMT4.

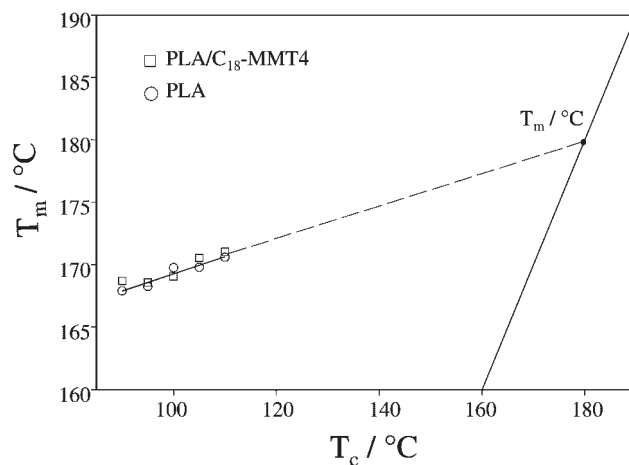


Figure 14. T_m versus T_c (Hoffman–Weeks) plots of pure PLA and PLA/C₁₈-MMT4.

The typical example of the time variation of the diameter of the spherulite D for pure PLA and PLA/C₁₈-MMT4 at higher T_c s is shown in Figure 15a, and the linear growth rate $G (= 1/2(dD/dt))$ of spherulite is summarized in Figure 15b.

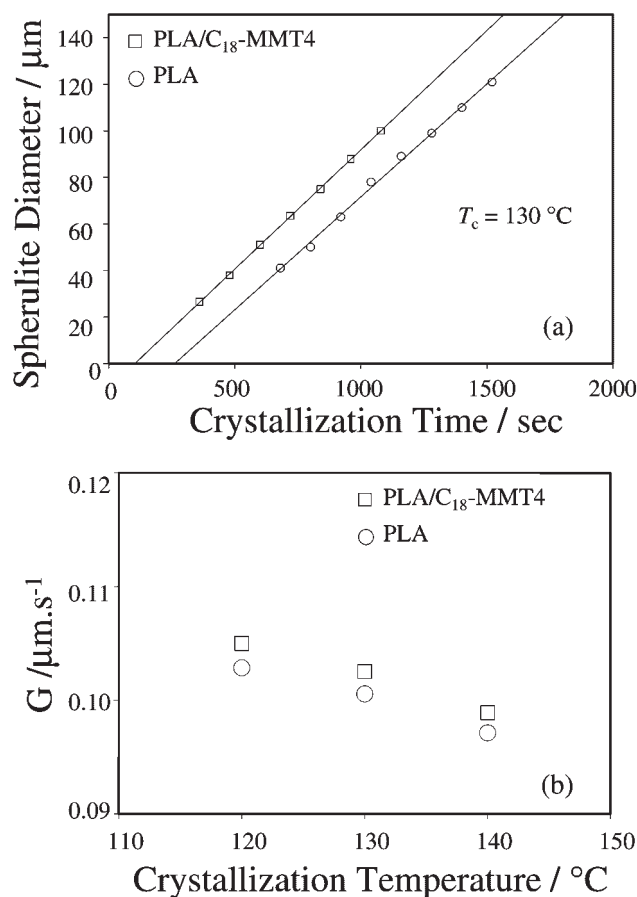


Figure 15. (a) Spherulite diameter as a function of crystallization time at $T_c = 130^\circ\text{C}$; (b) Linear growth rate of pure PLA and PLA/C₁₈-MMT4 as a function of T_c .

For both pure PLA and PLA/C₁₈-MMT4, G decreases with increasing T_c in the temperature range of 120–140 °C. However, for PLA/C₁₈-MMT4, G shows a slightly higher value compared with that of pure PLA. This observation indicates that the dispersed C₁₈-MMT particles have no effect on the crystallization, and no big acceleration of G in the crystallization of the PLA/C₁₈-MMT4.^[52] This observation suggests that the diffuse rate of bulk PLA molecules is not enhanced with the addition of C₁₈-MMT for every temperature of measurement, so that the overall crystallization rate is affected only by nucleation of the C₁₈-MMT particles.^[33,53]

From Figure 16, the number of heterogeneous nuclei N can be estimated from a rough approximation using Equation 4. The calculated value of N at 130 °C is $9.3 \times 10^{-7} \mu\text{m}^{-3}$ for pure PLA and $55.7 \times 10^{-7} \mu\text{m}^{-3}$ for PLA/C₁₈-MMT4. The time variation of the volume fraction of the spherulites increases in proportion to NG^3 (\cong overall crystallization rate). This fact suggests that the overall crystallization rates of the PLA/C₁₈-MMT4 at high temperature ($T_c = 130$ °C) are about half an order of magnitude higher than that of the matrix PLA without C₁₈-MMT. The difference of N between pure PLA and PLA/C₁₈-MMT4 at $T_c = 130$ °C is higher than that at low T_c . This observation suggests that the PLA/C₁₈-MMT4 exhibits heterogeneous nucleation kinetics, which depend on more originating from the well-dispersed C₁₈-MMT particles in the matrix at high temperature. Here, we should be mentioned that the spherulites of PLA/C₁₈-MMT4 have a lower order than that of pure PLA due to the dispersed C₁₈-MMT particles in the spherulites.^[48] Hence, the aggregated C₁₈-MMT particles, which are not nucleated during crystallization, exist inside the spherulite, and then the regular orientation of the lamella stacks inside the spherulites may be disturbed.

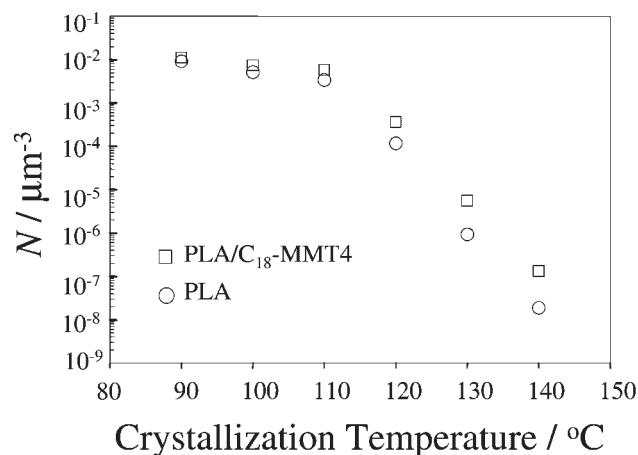


Figure 16. Nucleation density N of pure PLA and PLA/C₁₈-MMT4 as a function of T_c .

Melt Rheology

PLA/OMLS nanocomposites show improved material properties such as higher modulus, decreased barrier properties, increased biodegradability, and various other properties in comparison with the virgin PLA. In order to understand the processability of these materials, that is, the final stage of any polymeric material, one must understand the detailed rheological behavior of these materials in the molten state. Understanding the rheological properties of nanocomposite melts is not only important in gaining fundamental knowledge of the processability, but is also helpful in understanding the structure–property relationships in these materials. In this section we will describe the melt rheological properties of pure PLA and PLA/C₁₈-MMT nanocomposites in detail. PLA/C₁₈-MMT with three different amounts of C₁₈-MMT of 3, 5, and 7 wt.-% were correspondingly abbreviated as PLA/C₁₈-MMT3, PLA/C₁₈-MMT5, and PLA/C₁₈-MMT7, respectively.^[25a]

Dynamic Oscillatory Shear Measurements

Generally, the rheology of polymer melts depends strongly on the temperature at which the measurement is carried out. It is well known that for thermo-rheologically simple materials, bilogarithmic plots of the isotherms of the storage modulus, $G'(\omega)$, loss modulus $G''(\omega)$, and complex viscosity ($|\eta^*(\omega)|$) can be superimposed by horizontal shifts $\log(a_T)$, along the $\log(a_T\omega)$ axis, and vertical shifts given by $\log(b_T)$ such that:^[54]

$$\begin{aligned} b_T G'(a_T \omega, T_{\text{ref}}) &= b_T G'(\omega, T) \\ b_T G''(a_T \omega, T_{\text{ref}}) &= b_T G''(\omega, T) \\ (b_T/a_T) |\eta^*(a_T \omega, T_{\text{ref}})| &= |\eta^*(\omega, T) \end{aligned}$$

T_{ref} is the reference temperature. All isotherms measured for pure PLA and for various PLA/C₁₈-MMT nanocomposites can be superimposed in this way.

In case of polymer samples, it is expected that, at the temperatures and frequencies at which the rheological measurements were carried out, characteristic homopolymer-like terminal flow behavior should be exhibited, expressed by a power-law of $G'(\omega) \propto \omega^2$ and $G''(\omega) \propto \omega$.

The master curves for $G'(\omega)$ and $G''(\omega)$ of pure PLA and three different PLA/C₁₈-MMT nanocomposites with different wt.-% of C₁₈-MMT loading are presented in Figure 17. At high frequencies ($a_T\omega > 10$), the viscoelastic behavior of all nanocomposites is the same. On the other hand, at low frequencies ($a_T\omega < 10$), both moduli exhibit weak frequency dependence with increasing C₁₈-MMT content, which means that there are gradual changes of behavior from liquidlike [$G'(\omega) \propto \omega^2$ and $G''(\omega) \propto \omega$] to solidlike with increasing C₁₈-MMT content.

The terminal regions slope of the master curves for $G'(\omega)$ and $G''(\omega)$ are presented in Table 5. The slope of $G'(\omega)$ and $G''(\omega)$ in the terminal region of the master curves of PLA

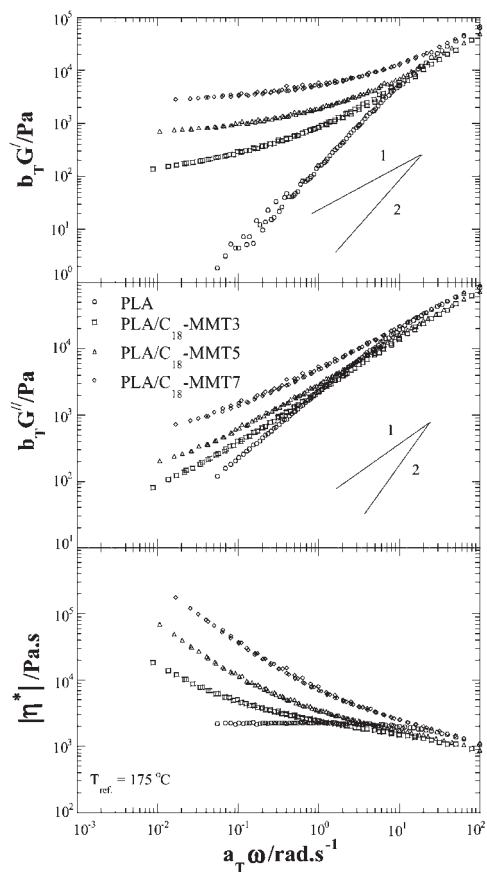


Figure 17. Reduced frequency dependence of the storage modulus (G'), loss modulus (G''), and complex viscosity [$|\eta^*|(\omega)$] of pure PLA and various PLA/ C_{18} -MMT nanocomposites.

matrix is 1.85 and 1, respectively, and these values are in the range expected for polydisperse polymers.^[55] On the other hand, the slopes of $G'(\omega)$ and $G''(\omega)$ are considerably lower for all PLA/ C_{18} -MMT nanocomposites compared with those of pure PLA. In fact, for PLA/ C_{18} -MMT nanocomposites with high C_{18} -MMT content, $G'(\omega)$ becomes nearly independent at low $a_T\omega$ and exceeds $G''(\omega)$, characteristic of materials exhibiting a pseudo-solidlike behavior.

As seen in Table 3, ξ_{LS} value of nanocomposite is smaller than that of L_{LS} suggesting the formation of 'spatially-linked structure'. According to this structure, the individual stacked silicate layers are incapable of freely rotating (only translational motion is available), and hence, the relaxations of the structure by imposing a small ω is prevented almost completely with high C_{18} -MMT content.^[54] This

Table 5. Terminal regions of slopes of $G'(\omega)$ and $G''(\omega)$.

Sample	$G'(\omega)$	$G''(\omega)$
PLA	1.85	1
PLA/ C_{18} -MMT3	0.25	0.5
PLA/ C_{18} -MMT5	0.18	0.4
PLA/ C_{18} -MMT7	0.1	0.3

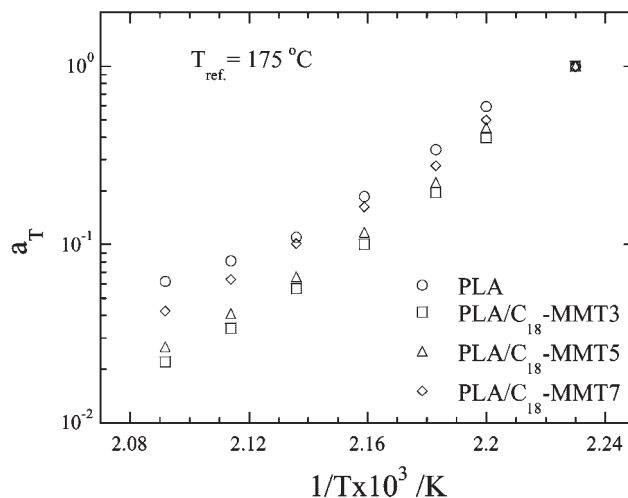


Figure 18. Frequency shift factors of pure PLA and various PLA/ C_{18} -MMT nanocomposites.

type of prevented relaxation due to the highly geometric constraints or physical jamming of the stacked and intercalated silicate layers led to the presence of pseudo-solidlike behavior as observed in the cases of PLA/ C_{18} -MMT nanocomposites. The formation of this type of *spatially-linked-structure* in the PLA/ C_{18} -MMT nanocomposite with high C_{18} -MMT content in the molten state is also confirmed by the lower slope values of the dynamic moduli in the case of PLA/ C_{18} -MMT nanocomposites.^[54,56]

The temperature-dependent frequency shift factor, a_T , used to generate the master curves is shown in Figure 18. The dependence of a_T on the C_{18} -MMT loading suggests that the temperature-dependent relaxations processes of the pure PLA melt observed in the viscoelastic measurements are somehow affected by the presence of silicate layers,^[54] and deviation is significant with low C_{18} -MMT content.

Figure 19 represents the C_{18} -MMT content dependent (wt.-%) flow activation energy (E_a) of pure PLA and various

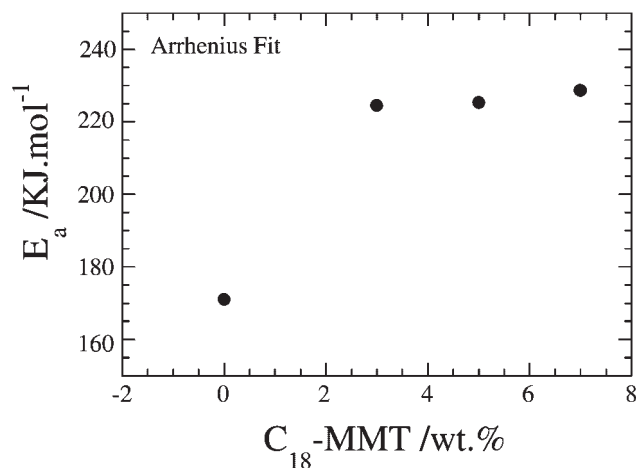


Figure 19. Flow activation energy of pure PLA and various PLA/ C_{18} -MMT nanocomposites as a function of C_{18} -MMT content.

nanocomposites obtained from an Arrhenius fit^[25a] of master curves. There is a significant increase of E_a for PLA/ C_{18} -MMT3 compared with that of pure PLA followed by a much slower increase with increasing C_{18} -MMT content. This behavior may be due to the dispersion of intercalated and stacked C_{18} -MMT silicate layers in the PLA matrix.

The dynamic complex viscosity $[|\eta^*|(\omega)]$ master curves for the pure PLA and various PLA/ C_{18} -MMT nanocomposites, based on linear dynamic oscillatory shear measurements, are also presented in Figure 17. From Figure 17, we can see at low $a_T\omega$ region ($< 10 \text{ rad}\cdot\text{s}^{-1}$), pure PLA exhibits almost Newtonian behavior while all nanocomposites show a very strong shear-thinning tendency. The high viscosity of PLA/ C_{18} -MMT nanocomposite can be explained by the flow restrictions of polymer chains in the molten state due to the presence of MMT particles.

We believe this behavior comes from the nature of the layered silicate particles, which are dispersed in the PLA matrix. In our previous study^[57] on lyophilized smectic layered silicate-toluene suspensions, we observed this type of shear thinning feature of the silicate particles in the rapid shear flow. Such a feature is strongly dependent on the shear rate in the dynamic measurements because of the formation of the shear-induced alignment of the dispersed silicate particles.^[57]

Steady Shear Measurements

The steady-shear rheological behavior of pure PLA and a series of intercalated PLA/ C_{18} -MMT nanocomposites are shown in Figure 20. The shear-viscosity of nanocomposites is enhanced considerably at all shear rates with time and at a fixed shears rate increases monotonically with increasing silicate loading. On the other hand, all intercalated nanocomposites exhibit strong rheoexy behavior,^[54] and this behavior becomes prominent at low shear rate ($\dot{\gamma} = 0.001 \text{ s}^{-1}$), while pure PLA exhibits a time-independent viscosity at all shear rates. With increasing shear rates, the shear viscosity attains a plateau after a certain time (indicated with the arrows in figure), and the time required to attain this plateau decreases with increasing shear rates. The possible reason for this type of behavior may be due to the planer alignment of the silicate particles towards the flow direction under shear. When shear rate is very slow (0.001 s^{-1}), silicate particles take a longer time to attain complete planer alignment along the flow direction, and this measurement time (1000 s) is too short to attain such alignment. For this reason, nanocomposites show strong rheoexy behavior. On the other hand, under slightly higher shear rates (0.005 s^{-1} or 0.01 s^{-1}), this measurement time is considerable enough to attain such an alignment, and hence, nanocomposites show time-independent shear viscosity after a certain time.

In Figure 21, we show shear rates dependence of viscosity for pure PLA and various PLA/ C_{18} -MMT nanocom-

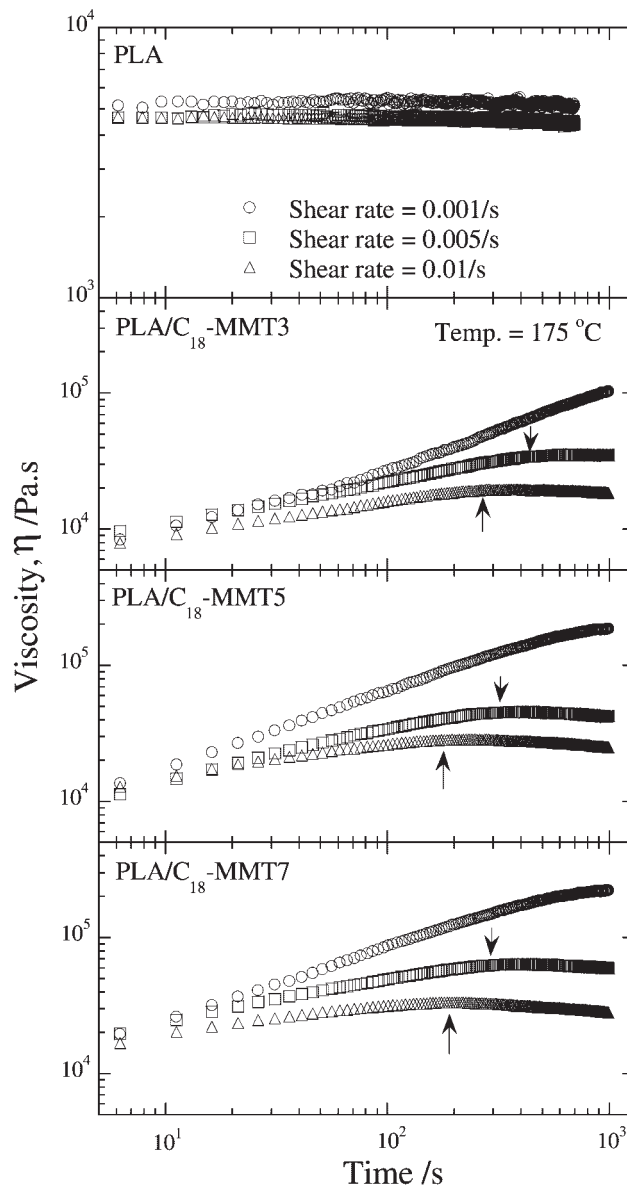


Figure 20. Steady shear viscosity of pure PLA and PLA/ C_{18} -MMT nanocomposites as function of time.

posites measured at $175 \text{ }^\circ\text{C}$. While the pure PLA exhibits almost Newtonian behavior at all shear rates, whereas nanocomposites exhibited non-Newtonian behavior. At very low shear rates, shear viscosity of nanocomposites initially exhibits some shear-thickening behavior, and this corresponds to rheoexy as observed at very low shear rates (see Figure 20). After that, all nanocomposites show a very strong shear-thinning behavior at all measured shear rates, and this behavior is analogous to the results obtained in the case of the oscillatory shear measurements (see Figure 17). Additionally, at very high shear rates, the steady shear viscosities of nanocomposites are comparable to those of pure PLA. These observations suggest that the silicate

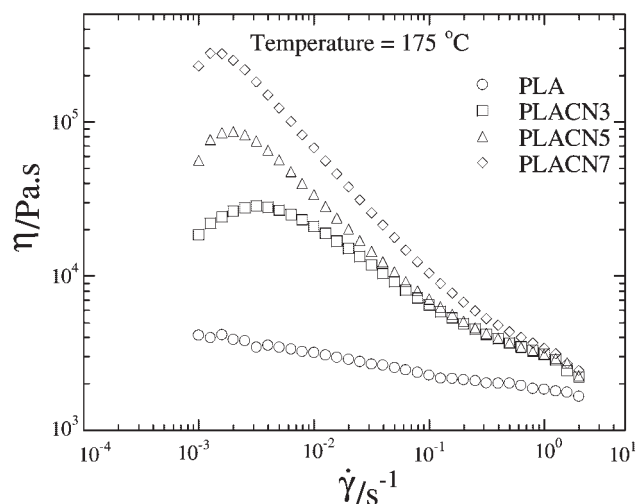


Figure 21. Steady shear viscosity of pure PLA and PLA/C₁₈-MMT nanocomposites as function of shear rate.

layers are strongly oriented towards the flow direction at high shear rates, and shear thinning behavior at high shear rates is dominated by that of pure polymer.^[58]

Like the other polymer/OMLS systems,^[54,56,59] the data for PLA/C₁₈-MMT nanocomposites also exhibit significant deviation from the Cox–Merz relation,^[60] while pure PLA nicely obeys the empirical Cox–Merz relation, which requires that for the $\dot{\gamma} = \omega$, the viscoelastic data should obey the relationship $\eta(\dot{\gamma}) = |\eta^*(\omega)|$. There are two possible reasons for the deviation of the Cox–Merz relation in the case of nanocomposites: First of all this rule is only applicable for homogeneous systems like homopolymer melts, but nanocomposites are heterogeneous systems. For this reason, this relation is nicely obeyed in the case of pure PLA. Secondly, the structure formation is different when nanocomposites are subjected to dynamic oscillatory shear and steady shear measurements.

Elongational Flow Behavior

Figure 22a shows double-logarithmic plots of transient elongational viscosity (η_E) against time (t) observed for PLA/C₁₈-MMT5 containing 5 wt.-% of C₁₈-MMT at 170 °C with different Hencky strain rates ($\dot{\epsilon}_0$) ranging from 0.01 to 1 s⁻¹. We see in a very strong tendency of *strain-induced hardening* for PLA/C₁₈-MMT5 melt. In the early stage, η_E gradually increases with t but is almost independent of $\dot{\epsilon}_0$, which we generally call the *linear region* of the viscosity curve. After a certain time, t_{η_E} which we call the *up-rising* time (marked with the upward arrows in figure), strongly dependent on $\dot{\epsilon}_0$, we see rapid upward deviation of η_E from the curves of the linear region. On the other hand, we have tried to measure the elongational viscosity of pure PLA but we were unable to do that accurately. We believe very low shear viscosity of pure PLA is the main reason for this,

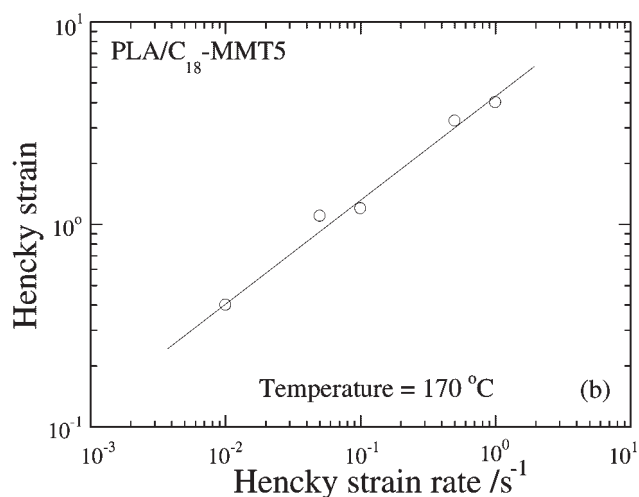
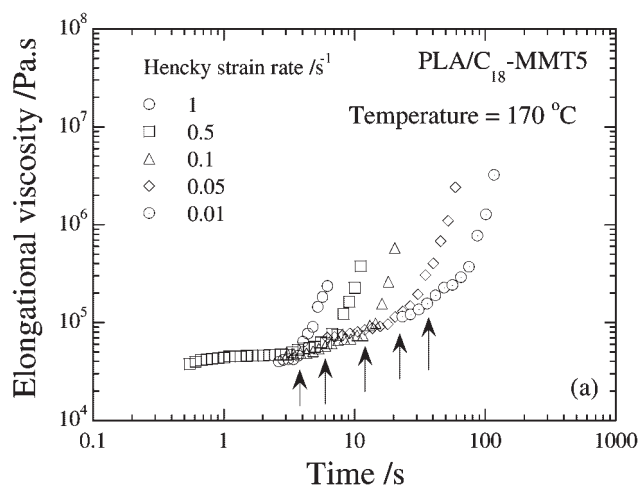


Figure 22. (a) Time variation of elongational viscosity for PLA/C₁₈-MMT5 melt at 170 °C; (b) Strain rate dependence of up-rising Hencky strain.

because minimum viscosity range of our instrument is greater than 10⁻⁴ Pa · s⁻¹. However, we have confirmed that neither strain-induced hardening in elongation nor rheopecty in shear flow (see Figure 19 and Figure 20) took place in the case of pure PLA having slightly higher molecular weights and polydispersity with that of PLA/C₁₈-MMT5.^[25a,61]

Like polypropylene/OMLS systems, the extended Trouton rule, $3\eta_0(\dot{\gamma}; t) \cong \eta_E(\dot{\epsilon}_0; t)$, also does not hold for PLA/C₁₈-MMT5 melts, as opposed to the melt of pure polymers.^[62] These results indicate that in the case of PLA/C₁₈-MMT5, the flow induced internal structural changes also occur in elongation flow,^[61,62] but the changes are quite different from shear flow. The strong rheopecty observed in shear measurements for PLA/C₁₈-MMT5 at very slow shear rate reflects the fact that the shear-induced structural change involved a process with an extremely long relaxation time.

As to the elongation-induced structure development, we show in Figure 22b Hencky strain rate dependence of the up-rising Hencky strain ($\varepsilon_{\eta_E} = \dot{\varepsilon}_0 \times t_{\eta_E}$) taken for PLA/C₁₈-MMT5 at 170 °C. The ε_{η_E} increases systematically with $\dot{\varepsilon}_0$. The lower the value of $\dot{\varepsilon}_0$, the smaller the value of ε_{η_E} . This tendency probably corresponds to the rheopecty of PLA/C₁₈-MMT5 under slow shear flow.

Foam Processing and Cellular Structure

In the preceding sections, we have reported rheological properties of pure PLA and various PLA/C₁₈-MMT nanocomposites in detail. Dynamic measurements indicated the formation of a *spatially-linked-structure* in the case of PLA/C₁₈-MMT nanocomposite melts, and during shear measurements we observed very strong rheopecty behavior of PLA/C₁₈-MMT nanocomposite melts under very slow shear field. Under uniaxial elongation flow, PLA/C₁₈-MMT nanocomposite melts exhibited very high viscosity and a tendency of strong strain-induced hardening, which we believe may originate from the perpendicular alignment of the silicate layers towards the stretching direction.^[62] This strain-induced hardening behavior is an indispensable characteristic for foam processing due to its capacity to withstand the stretching force experienced during the latter stages of bubble growth. To evaluate the performance potential of the biodegradable PLA/C₁₈-MMT nanocomposite towards foam application, we have conducted the foam processing of one representative nanocomposite, PLA/C₁₈-MMT by a newly developed pressure cell technique with the expectation that they would provide advanced biodegradable foam with excellent properties, meeting our demand.^[63]

Figure 23a shows the typical results of SEM images of the freeze-fracture surfaces of pure PLA and PLA/C₁₈-MMT5 foams. We have noted here that homogeneous cells with close-cell structure were formed in the case of PLA/C₁₈-MMT5 foam, while the pure PLA foam shows nonuniform cell structure having large cell size ($\sim 230 \mu\text{m}$). Also, the PLA/C₁₈-MMT5 foam shows a smaller cell size (d) and larger cell density (N_c) compared with pure PLA foam, suggesting that the dispersed silicate particles act as nucleating sites for cell formation.^[20]

In the case of nanocomposite foam, we calculated the distribution function of cell size from SEM image, and this is presented in Figure 23b. The PLA/C₁₈-MMT5 foam nicely obeyed the Gaussian distribution. From the SEM images, we have quantitatively calculated various morphological parameters such as d , δ , N_c , and so on for the PLA/C₁₈-MMT5 foam, and the values are 2.59 μm , 0.66 μm , and $3.6 \times 10^{11} \text{ cell} \cdot \text{cm}^{-3}$, respectively.^[63]

These results indicate that the presence of MMT particles plays a very vital role in controlling the size of cell during foaming.^[63] On the other hand, the very high value of N_c in the case of the PLA/C₁₈-MMT5 foam indicates that the final ρ_f is controlled by the competitive processes in the cell

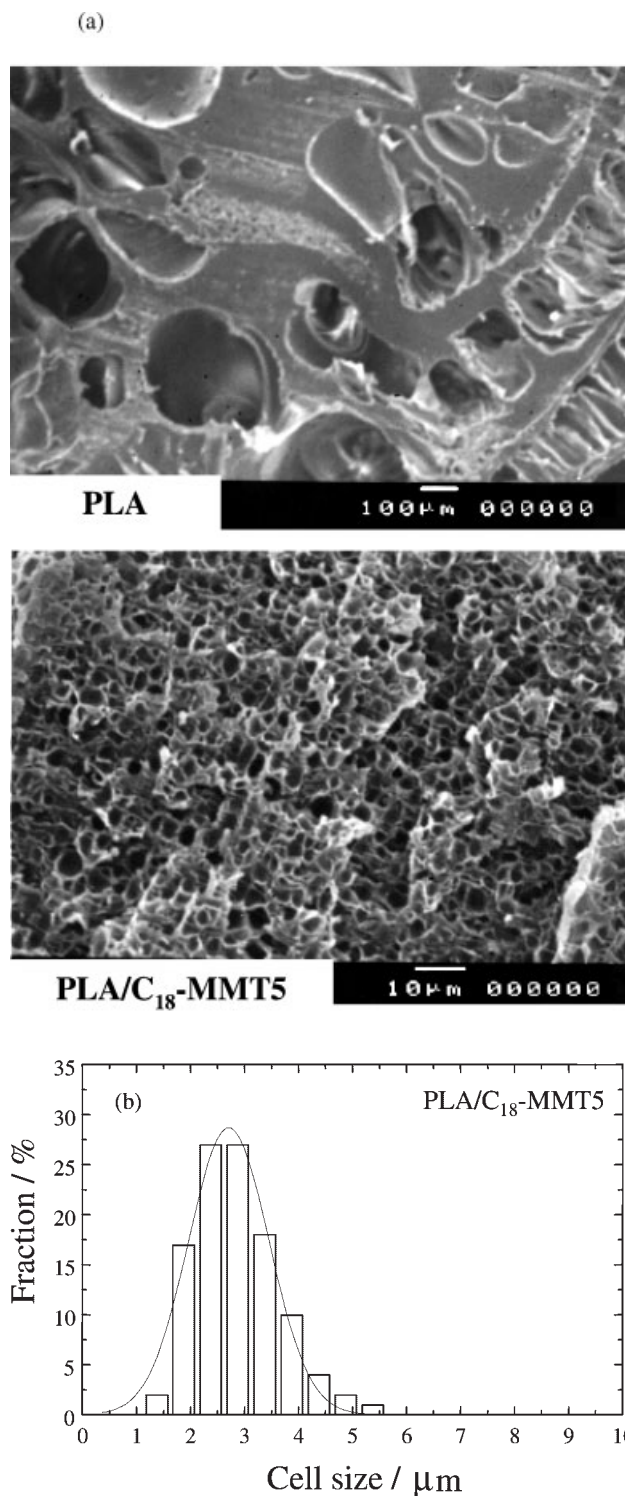


Figure 23. (a) SEM image of freeze fracture surface of pure PLA and PLA/C₁₈-MMT5 foams; (b) Cell size distribution of PLA/C₁₈-MMT5 foam. Average values of d in μm and variances σ_d^2 in μm^2 in the Gaussian fit through the data are 2.59 and 0.551, respectively.

nucleation, its growth, and coalescence. The cell nucleation, in the case of nanocomposite systems, took place in the boundary between the matrix polymer and the dispersed silicate particles. For this reason, the cell growth and coalescence are strongly affected by the storage and loss modulus (\cong viscosity component) of the materials during processing.

Even though the foam processing in this study was conducted below T_m of the matrix, in presence of supercritical CO_2 , the material became soft. For this reason, we have to take into account not only the MMT effect on N_c and the moduli but also the strain-induced hardening on the formed thick cell wall during foam processing in order to understand the above features on the nanocomposite foam. Such strain-induced hardening behavior is probably strong enough to increase the extensional viscosity under biaxial flow and to protect the cell from the breakage at high temperature; therefore, the strain-induced hardening led to the formation of homogeneous micro-cellular foam in the case of the PLA/ C_{18} -MMT5 nanocomposite without the loss of mechanical properties.^[63,64]

Conclusion

In this article, we have described various technologies have been used to produce PLA and a brief insight into the versatility of nanocomposite technology. We have successfully prepared a series of biodegradable PLA/OMLS nanocomposites by simple melt extrusion of PLA and OMLS, wherein silicate layers of OMLS are either intercalated, intercalated-and-flocculated, partly exfoliated, or a mixture of all three. All the nanocomposites exhibited

dramatic improvement in mechanical and various materials properties concurrently as compared with those of pure PLA. These improvements include mechanical and flexural properties, heat distortion temperature, oxygen gas permeability, and the rate of crystallization, with a simultaneous improvement in biodegradability.

We have also investigated in detail the melt rheological properties for representative organically modified layered silicate based nanocomposites of polylactide. At low frequencies, both dynamic moduli exhibit weak frequency dependence with increasing C_{18} -MMT content, which means that there are gradual changes of behavior from liquidlike to solidlike with increasing C_{18} -MMT content. We have established that this behavior is due to the formation of mesoscopic structure of randomly oriented intercalated and stacked silicate layers in the PLA matrix. In the case of steady-shear measurements we observed very strong rheopecty behavior of nanocomposites in a very slow shear field.

Under uniaxial elongational flow, PLA/ C_{18} -MMT5 melts exhibited very high viscosity and a tendency of strong strain-induced hardening, which we believe may be originated from the perpendicular alignment of the silicate layers towards the stretching direction. On the basis of these rheological data, we have conducted foam processing of one representative nanocomposite by a newly developed pressure cell technique using carbon dioxide as a physical blowing agent. Nanocomposite foam shows homogeneous close-cell structures having cell sizes in the micrometer region ($2.59 \mu\text{m}$).

These are entirely new types of composite materials based on plant and natural materials (OMLS). When

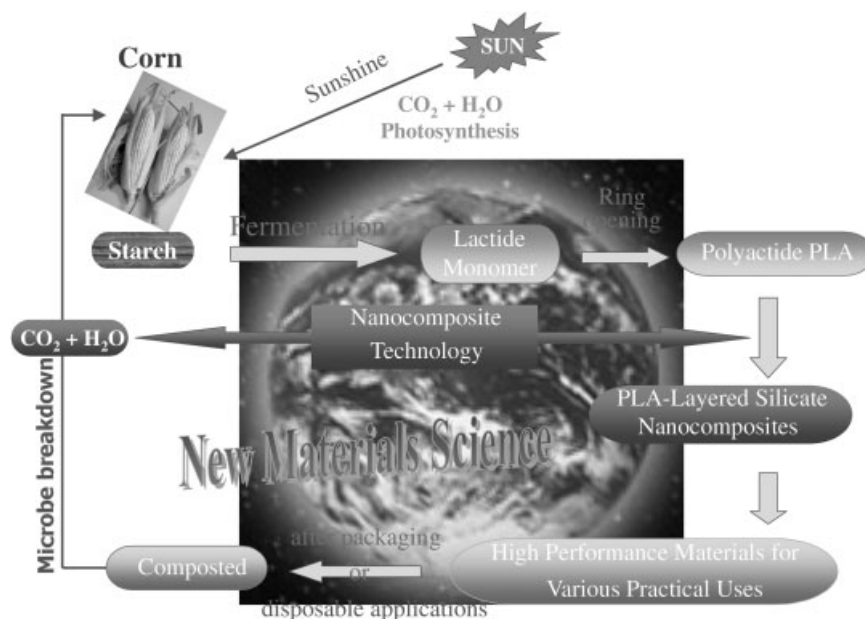


Figure 24. Schematic illustration of the main concepts of this paper.

disposed of in compost, these are safely decomposed into carbon dioxide, water, and humus through the activity of microorganisms. The carbon dioxide and water will become corn or sugarcane again through plant photosynthesis (see Figure 24). Thus, these materials have a great deal of future promise for potential applications as high-performance biodegradable materials (already commercially available through Unitika Ltd., Japan), and open up a new dimension for plastic and composite materials.

Acknowledgement: Thanks are due to the *Japan Society for the Promotion of Science* for awarding a postdoctoral fellowship and a research grant to S. Sinha Ray (ID No. P02152). The authors thank Dr. J. Y. Nam, Mr. K. Yamada, Mr. A. Ogami, and Dr. K. Ueda for their valuable contribution to this manuscript. We also express our appreciation to the reviewers for their constructive and meticulous assessment of the manuscript.

- [1] R. E. Drumright, P. R. Gruber, D. E. Henton, *Adv. Mater.* **2000**, *12*, 1841.
- [2] J. Lunt, *Polym. Degrad. Stabil.* **1998**, *59*, 145.
- [3] Q. Fang, M. A. Hanna, *Ind. Crops Prod.* **1999**, *10*, 47.
- [4] Kanebo Ltd., Japan, website: www.kanebotx.com (accessed Aug 27, 2002).
- [5] S. Sinha Ray, M. Okamoto, *Prog. Polym. Sci.* **2003**, in press.
- [6] M. Biswas, S. Sinha Ray, *Adv. Polym. Sci.* **2001**, *155*, 167.
- [7] M. Alexander, P. Dubois, *Mater. Sci. Eng. R.* **2000**, *28*, 1.
- [8] E. P. Giannelis, R. Krishnamoorti, E. Manias, *Adv. Polym. Sci.* **1999**, *138*, 107.
- [9] J. S. Chen, M. D. Poliks, C. K. Ober, Y. Zhang, U. Wiesner, E. P. Giannelis, *Polymer* **2002**, *43*, 4895.
- [10] N. Ogata, G. Jimenez, H. Kawai, T. Ogihara, *J. Polym. Sci. Part B: Polym. Phys.* **1997**, *35*, 389.
- [11] S. Bandyopadhyay, R. Chen, E. P. Giannelis, *Polym. Mater. Sci. Eng.* **1999**, *81*, 159.
- [12] [12a] M.-A. Paul, M. Alexandre, P. Degee, C. Calberg, R. Jerome, P. Dubois, *Macromol. Rapid Commun.* **2003**, *24*, 561; [12b] J.-H. Chang, Y. U. An, G. S. Sur, *J. Polym. Sci. Part B: Polym. Phys.* **2003**, *41*, 94; [12c] M.-A. Paul, M. Alexandre, P. Degee, C. Henrist, A. Rulmont, P. Dubois, *Polymer* **2003**, *44*, 443; [12d] M. Pluta, A. Galeski, M. Alexandre, M.-A. Paul, P. Dubois, **2001**, *86*, 1497.
- [13] US 5 142 023 (1992) (to Cargill), invs.: P. R. Gruber, E. S. Hall, J. J. Kolstad, M. L. Iwen, R. D. Benson, R. L. Borchardt.
- [14] US 5 310 865 (1994) (to Mitsui Tuatsu), invs.: K. Enomoto, M. Ajioka, A. Yamaguchi.
- [15] P. H. Nam, P. Maiti, M. Okamoto, T. Kotaka, N. Hasegawa, A. Usuki, *Polymer* **2001**, *42*, 9633.
- [16] E. W. Fisher, H. J. Sterzel, G. Wegner, *Kolloid Z. Z. Polym.* **1973**, *25*, 980.
- [17] M. Okamoto, H. Kubo, T. Kotaka, *Macromolecules* **1998**, *31*, 4223.
- [18] T. Kotaka, A. Kojima, M. Okamoto, *Rheol. Acta* **1997**, *36*, 646.
- [19] J. Meissner, J. Hostettler, *Rheol. Acta* **1994**, *33*, 1.
- [20] [20a] M. Okamoto, P. H. Nam, P. Maiti, T. Kotaka, T. Nakayama, M. Takada, M. Ohshima, A. Usuki, N. Hasegawa, H. Okamoto, *Nano Lett.* **2001**, *1*, 503; [20b] P. H. Nam, P. Maiti, T. Kotaka, M. Okamoto, T. Nakayama, M. Takada, M. Ohshima, A. Usuki, N. Hasegawa, H. Okamoto, *Polym. Eng. Sci.* **2002**, *42*, 1907.
- [21] R. A. Vaia, K. D. Jandt, E. J. Kramer, E. P. Giannelis, *Chem. Mater.* **1996**, *8*, 2628.
- [22] V. A. Dritis, C. Tchoubar, *X-ray Diffraction by Disordered Lamellar Structures*, Springer, New York 1990, p. 21.
- [23] [23a] B. D. Cullity, *Principles of X-ray Diffraction*; Addison-Wesley: Reading, MA, 1978; [23b] R. E. Klimentidis, I. D. R. Mackinnon, *Clays Clay Miner.* **1986**, *34*, 155.
- [24] Since the silicate layers are comprised of heavier elements (Al, Si, O) than the interlayer and surrounding matrix (C, H, N, etc.), they appeared darker in bright field images.
- [25] [25a] S. Sinha Ray, P. Maiti, M. Okamoto, K. Yamada, K. Ueda, *Macromolecules* **2002**, *35*, 3104; [25b] S. Sinha Ray, K. Okamoto, K. Yamada, M. Okamoto, *Nano Lett.* **2002**, *2*, 423.
- [26] S. Sinha Ray, K. Yamada, M. Okamoto, K. Ueda, *J. Nanosci. Nanotech.* **2003**, *3*, in press.
- [27] S. Sinha Ray, K. Yamada, M. Okamoto, K. Ueda, *Polymer* **2003**, *44*, 857.
- [28] P. Maiti, K. Yamada, M. Okamoto, K. Ueda, K. Okamoto, *Chem. Mater.* **2002**, *14*, 4654.
- [29] S. Sinha Ray, K. Yamada, A. Ogami, M. Okamoto, K. Ueda, *Macromol. Rapid Commun.* **2002**, *23*, 943.
- [30] S. Sinha Ray, K. Yamada, M. Okamoto, A. Ogami, K. Ueda, *Chem. Mater.* **2003**, *15*, 1456.
- [31] B. Wunderlich, *Macromolecular Physics*, Academic Press, New York 1976, Vol. 2, p. 363.
- [32] B. Eling, S. Gogolewski, A. J. Pennings, *Polymer* **1977**, *23*, 1587.
- [33] P. Maiti, P. H. Nam, M. Okamoto, A. Usuki, N. Hasegawa, *Macromolecules* **2002**, *35*, 2042.
- [34] S. Sinha Ray, K. Okamoto, P. Maiti, M. Okamoto, *J. Nanosci. Nanotech.* **2002**, *2*, 171.
- [35] P. Maiti, M. Okamoto, *Macromol. Mater. Eng.* **2003**, *288*, 440.
- [36] L. Nielsen, *J. Macromol. Sci. Chem.* **1967**, *A1(5)*, 929.
- [37] A. A. Gusev, H. R. Lusti, *Adv. Mater.* **2001**, *13*, 1641.
- [38] S. Sinha Ray, K. Yamada, M. Okamoto, Y. Fijumoto, A. Ogami, K. Ueda, *Polymer* **2003**, *44*, in press.
- [39] M. S. Reeve, S. P. MaCarthy, M. J. Downey, R. A. Gross, *Macromolecules* **1994**, *27*, 825.
- [40] T. Iwata, Y. Doi, *Macromolecules* **1998**, *31*, 2461.
- [41] M. Hakkarainen, S. Karlsson, A.-C. Albertsson, *Polymer* **2000**, *41*, 2331.
- [42] S. Sinha Ray, K. Yamada, M. Okamoto, K. Ueda, *Nano Lett.* **2002**, *2*, 1093.
- [43] S. Sinha Ray, K. Yamada, M. Okamoto, K. Ueda, *Macromol. Mater. Eng.* **2003**, *288*, 203.
- [44] S. Sinha Ray, K. Yamada, M. Okamoto, A. Ogami, K. Ueda, *Comp. Interfaces* **2003**, *10*, in press.
- [45] [45a] F. Kawai, *CRC Crit. Rev. Biotechnol.* **1987**, *6(3)*, 273; [45b] T. Taino, T. Fukui, Y. Shirakura, T. Saito, K. Tomita, T. Kaiho, S. Masamune, *Eur. J. Biochem.* **1982**, *124*, 71.
- [46] H. Kubo, H. Sato, M. Okamoto, T. Kotaka, *Polymer* **1998**, *39*, 501.
- [47] M. Okamoto, H. Kubo, T. Kotaka, *Polymer* **1998**, *39*, 3135.
- [48] J. Y. Nam, S. Sinha Ray, M. Okamoto, *Macromolecules* **2003**, *36*, in press.
- [49] M. Okamoto, T. Inoue, *Polymer* **1995**, *36*, 2736.
- [50] E. Martuscelli, S. Silvestre, G. Abate, *Polymer* **1982**, *23*, 229.

- [51] M. Okamoto, Y. Shinoda, N. Kinami, T. Okuyama, *J. Appl. Polym. Sci.* **1995**, *57*, 1055.
- [52] The low molecular weight of the PLA matrix in PLA/C₁₈-MMT4 is the main reason to observe the spherulites growth rate in the case of PLA/C₁₈-MMT4 because radial growth rate of the spherulites is inversely proportional to the degree of polymerization.
- [53] P. Maiti, P. H. Nam, M. Okamoto, N. Hasegawa, A. Usuki, *Polym. Eng. Sci.* **2002**, *42*, 1864.
- [54] S. Sinha Ray, K. Okamoto, M. Okamoto, *Macromolecules* **2003**, *36*, 2355.
- [55] B. Hoffmann, J. Kressler, G. Stoppelmann, Chr. Friedrich, G. M. Kim, *Colloid. Polym. Sci.* **2000**, *278*, 629.
- [56] K. Okamoto, S. Sinha Ray, M. Okamoto, *J. Polym. Sci. Part B: Polym. Phys.* **2003**, in press.
- [57] M. Okamoto, H. Taguchi, H. Sato, T. Kotaka, H. Tatayama, *Langmuir* **2000**, *16*, 4055.
- [58] R. Krishnamoorti, Y. Koray, *Curr. Opinion Colloid Interface. Sci.* **2001**, *6*, 464.
- [59] R. Krishnamoorti, J. Ren, A. S. Silva, *J. Chem. Phys.* **2001**, *114*, 4968.
- [60] W. P. Cox, E. H. Merz, *J. Polym. Sci.* **1958**, *28*, 619.
- [61] S. Sinha Ray, M. Okamoto, *Macromol. Mater. Eng.* **2003**, 288, in press.
- [62] M. Okamoto, P. H. Nam, P. Maiti, T. Kotaka, N. Hasegawa, A. Usuki, *Nano Lett.* **2001**, *1*, 295.
- [63] Y. Fujimoto, S. Sinha Ray, M. Okamoto, A. Ogami, K. Yamada, K. Ueda, *Macromol. Rapid Commun.* **2003**, *24*, 457.
- [64] M. Mitsunaga, Y. Ito, S. Sinha Ray, M. Okamoto, K. Hironaka, *Macromol. Mater. Eng.* **2003**, 288, 543.